The Astronomical Journal, 166:201 (26pp), 2023 November https://doi.org/10.3847/1538-3881/acfc1d

TOI-199 b: A Well-characterized 100 day Transiting Warm Giant Planet with TTVs Seen from Antarctica

Melissa J. Hobson[1,2], Trifon Trifonov[1,3,4], Thomas Henning[1], Andrés Jordán[2,5], Felipe Rojas[2,6], Nestor Espinoza[7], Rafael Brahm[2,5], Jan Eberhardt[1], Matías I. Jones[8], Djamel Mekarnia[9], Diana Kossakowski[1], Martin Schlecker[10], Marcelo Tala Pinto[2,5], Pascal José Torres Miranda[2,6], Lyu Abe[9], Khalid Barkaoui[11,12,13], Philippe Bendjoya[9], François Bouchy[14], Marco Buttu[15], Ilaria Carleo[13], Karen A. Collins[16], Knicole D. Colón[17], Nicolas Crouzet[18], Diana Dragomir[19], Georgina Dransfield[20], Thomas Gasparetto[21], Robert F. Goeke[22], Tristan Guillot[9], Maximilian N. Günther[23], Saburo Howard[9], Jon M. Jenkins[24], Judith Korth[25], David W. Latham[16], Monika Lendl[14], Jack J. Lissauer[26], Christopher R. Mann[27,28], Ismael Mireles[19], George R. Ricker[22], Sophie Saesen[14], Richard P. Schwarz[16], S. Seager[22,29,30], Ramotholo Sefako[31], Avi Shporer[22], Chris Stockdale[32], Olga Suarez[9], Thiam-Guan Tan[33], Amaury H. M. J. Triaud[20], Solène Ulmer-Moll[14,34], Roland Vanderspek[22], Joshua N. Winn[35], Bill Wohler[24,36], and George Zhou[37]

[1] Max-Planck-Institut für Astronomie, Königstuhl 17, D-69117 Heidelberg, Germany; hobson@mpia.de
[2] Millennium Institute for Astrophysics, Chile
[3] Department of Astronomy, Sofia University "St Kliment Ohridski," 5 James Bourchier Boulevard, BG-1164 Sofia, Bulgaria
[4] Zentrum für Astronomie der Universtät Heidelberg, Landessternwarte, Königstuhl 12, D-69117 Heidelberg, Germany
[5] Facultad de Ingeniería y Ciencias, Universidad Adolfo Ibáñez, Av. Diagonal las Torres 2640, Peñalolén, Santiago, Chile
[6] Instituto de Astrofísica, Facultad de Física, Pontificia Universidad Católica de Chile, Av. Vicuña Mackenna 4860, 782-0436 Macul, Santiago, Chile
[7] Space Telescope Science Institute, 3700 San Martin Drive, Baltimore, MD 21218, USA
[8] European Southern Observatory, Alonso de Córdova 3107, Vitacura, Casilla 19001, Santiago, Chile
[9] Université Côte d'Azur, Observatoire de la Côte d'Azur, CNRS, Laboratoire Lagrange, Bd de l'Observatoire, CS 34229, F-06304 Nice cedex 4, France
[10] Steward Observatory and Department of Astronomy, The University of Arizona, Tucson, AZ 85721, USA
[11] Astrobiology Research Unit, Université de Liège, 19C Allée du 6 Août, B-4000 Liège, Belgium
[12] Department of Earth, Atmospheric and Planetary Science, Massachusetts Institute of Technology, 77 Massachusetts Avenue, Cambridge, MA 02139, USA
[13] Instituto de Astrofísica de Canarias (IAC), Calle Vía Láctea s/n, E-38200, La Laguna, Tenerife, Spain
[14] Observatoire de Genève, Département d'Astronomie, Université de Genève, Chemin Pegasi 51b, 1290 Versoix, Switzerland
[15] INAF Osservatorio Astronomico di Cagliari, Via della Scienza 5, I-09047 Selargius CA, Italy
[16] Center for Astrophysics | Harvard & Smithsonian, 60 Garden Street, Cambridge, MA 02138, USA
[17] NASA Goddard Space Flight Center, 8800 Greenbelt Road, Greenbelt, MD 20771, USA
[18] Leiden Observatory, Leiden University, P.O. Box 9513, 2300 RA Leiden, The Netherlands
[19] Department of Physics and Astronomy, University of New Mexico, 210 Yale Boulevard NE, Albuquerque, NM 87106, USA
[20] School of Physics & Astronomy, University of Birmingham, Edgbaston, Birmingham B15 2TT, UK
[21] Institute of Polar Sciences—CNR, via Torino, 155, I-30172 Venice-Mestre, Italy
[22] Department of Physics and Kavli Institute for Astrophysics and Space Research, Massachusetts Institute of Technology, Cambridge, MA 02139, USA
[23] European Space Agency (ESA), European Space Research and Technology Centre (ESTEC), Keplerlaan 1, 2201 AZ Noordwijk, The Netherlands
[24] NASA Ames Research Center, Moffett Field, CA 94035, USA
[25] Lund Observatory, Division of Astrophysics, Department of Physics, Lund University, Box 43, SE-22100 Lund, Sweden
[26] Space Science & Astrobiology Division, MS 245-3, NASA Ames Research Center, Moffett Field, CA 94035, USA
[27] Département de Physique, Université de Montréal, Montréal, QC, Canada
[28] Trottier Institute for Research on Exoplanets (iREx), Canada
[29] Department of Earth, Atmospheric and Planetary Sciences, Massachusetts Institute of Technology, Cambridge, MA 02139, USA
[30] Department of Aeronautics and Astronautics, MIT, 77 Massachusetts Avenue, Cambridge, MA 02139, USA
[31] South African Astronomical Observatory, P.O. Box 9, Observatory, Cape Town 7935, South Africa
[32] Hazelwood Observatory, Australia
[33] Perth Exoplanet Survey Telescope, Perth, Western Australia
[34] Physikalisches Institut, University of Bern, Gesellschaftsstrasse 6, 3012 Bern, Switzerland
[35] Department of Astrophysical Sciences, Princeton University, 4 Ivy Lane, Princeton, NJ 08544, USA
[36] SETI Institute, Mountain View, CA 94043, USA
[37] University of Southern Queensland, Centre for Astrophysics, West Street, Toowoomba, QLD 4350, Australia
Received 2023 May 2; revised 2023 September 12; accepted 2023 September 19; published 2023 October 18

Abstract

We present the spectroscopic confirmation and precise mass measurement of the warm giant planet TOI-199 b. This planet was first identified in TESS photometry and confirmed using ground-based photometry from ASTEP in Antarctica including a full 6.5 hr long transit, PEST, Hazelwood, and LCO; space photometry from NEOSSat; and radial velocities (RVs) from FEROS, HARPS, CORALIE, and CHIRON. Orbiting a late G-type star, TOI-199 b has a $104.854^{+0.001}_{-0.002}$ day period, a mass of $0.17 \pm 0.02\ M_J$, and a radius of $0.810 \pm 0.005\ R_J$. It is the first warm exo-Saturn with a precisely determined mass and radius. The TESS and ASTEP transits show strong transit timing variations (TTVs), pointing to the existence of a second planet in the system. The joint analysis of the RVs and TTVs provides a unique solution for the nontransiting companion TOI-199 c, which has a period of

$273.69^{+0.26}_{-0.22}$ days and an estimated mass of $0.28^{+0.02}_{-0.01}$ M_J. This period places it within the conservative habitable zone.

Unified Astronomy Thesaurus concepts: Exoplanet astronomy (486); Exoplanet detection methods (489); Transit timing variation method (1710); Radial velocity (1332); Transit photometry (1709); Exoplanet systems (484)

1. Introduction

In the quest to understand how planets form and evolve, warm giant planets are a vital piece of the puzzle. Warm giants are generally defined as planets with sizes $R_p \geqslant 4\ R_\oplus$ and periods 10 days $\lesssim P \lesssim$ 300 days. Unlike their closer-in hot-Jupiter cousins, they are far enough from their host stars to not be strongly irradiated, and thus are not expected to be affected by radius inflation (see, e.g., Sarkis et al. 2020). Likewise, tidal circularization is not expected to impact their orbital parameters, meaning these can potentially be used to disentangle their migration history (see Dawson & Johnson 2018 for a review).

Identifying and characterizing a large sample of warm giants is the necessary first step toward understanding this population. Transiting warm giants around bright stars are especially valuable, as both their radii (via transits) and their masses (via radial velocities (RVs)) can be measured, and thus their densities computed and their internal structures modeled. The Transiting Exoplanet Survey Satellite mission (TESS; Ricker et al. 2015) is proving invaluable for the detection of these warm giants, with some 60 already published (according to the table of TESS planets on the NASA Exoplanet Archive,[38] as of 2023 February 6) and hundreds more expected from yield simulations of the prime and extended missions (Sullivan et al. 2015; Barclay et al. 2018; Kunimoto et al. 2022). Thanks primarily to TESS and its predecessor Kepler (Borucki et al. 2010), some 80 warm giants have had their radii and masses characterized to better than 25%, according to the TEPCAT catalog (Southworth 2011).[39] The majority of these are on the shorter end of the 10–300 day period range, with half having periods shorter than 20 days. Longer-period transiting warm giants remain rare. The Warm gIaNts with tEss collaboration (WINE; e.g., Brahm et al. 2019; Jordán et al. 2020; Schlecker et al. 2020; Hobson et al. 2021; Trifonov et al. 2021) seeks to confirm and characterize warm giant candidates from TESS, using a variety of photometric and spectroscopic facilities.

While the transit technique has been immensely fruitful, leading the list of planet discoveries with over 3900 of the over 5200 known exoplanets,[40] it is of necessity limited by orbital geometry—the planet must cross between the star and the observer—and biased toward short-period planets whose transits are more likely to be observed. However, for multi-planetary systems where the planets exert strong gravitational influences on each other, the transit timing variation (TTV; Agol et al. 2005; Holman & Murray 2005) technique can help to overcome these limitations in some cases: by measuring the TTVs for a transiting planet, we can detect nontransiting planets, and measure the masses of all bodies involved. The first detection of the TTV effect was for Kepler-19 b by Ballard et al. (2011), but they could not unambiguously determine the mass and period of the nontransiting companion. The first planet with a unique solution determined from TTVs was KOI-872 c (Nesvorný et al. 2012). Since then, this technique has enabled the detection of 24 planets,[41] many of which are warm giants (e.g., Trifonov et al. 2021; a pair of warm giants where only the inner one transits).

In this paper, we present the TOI-199 system, consisting of two giant planets. The inner planet is transiting, with a period of $104.854^{+0.001}_{-0.002}$ days, and was found in TESS photometry. The outer planet does not transit, but was revealed by the TTVs that it induces on the transits of the inner planet. The paper is organized as follows. We present the observational data in Section 2. In Section 3 we analyze the data, and characterize the star and planets. Our results are discussed in Section 4, and finally, we provide our conclusions in Section 5.

2. Observations

2.1. TESS Photometry

TOI-199 was observed by the TESS prime and first and second extended missions between 2018 July 25 and 2023 April 06, in Sectors 1–13, 27, 29–37, 39, and 61–63, using camera 4. Sector 1 was observed with CCD 4; Sectors 2, 3, and 4 with CCD 1; Sectors 5, 6, and 7 with CCD 2; Sectors 8, 9, 10, and 11 with CCD 3; Sectors 12, 13, and 27 with CCD 4; Sectors 29, 30, and 31 with CCD 1; Sectors 32, 33, and 34 with CCD 2; Sectors 35, 36, and 37 with CCD 3; Sector 39 with CCD 4; Sector 61 with CCD 2; and Sectors 62 and 63 with CCD 3.

The 2 minute cadence data for TOI-199 were processed by the TESS Science Processing Operation Center (SPOC; Jenkins et al. 2016) at NASA Ames Research Center. A potential transit signal was identified in the SPOC transit search (Jenkins 2002; Jenkins et al. 2010, 2020) of the light curve, and designated as a TESS Object of Interest (TOI) by the TESS Science Office based on SPOC data validation results (Twicken et al. 2018; Li et al. 2019) indicating that it was consistent with a transiting planet. The SPOC difference image centroiding analysis locates the source of the transit signal to within $1\farcs0 \pm 2\farcs5$ of the target star's catalog position (Twicken et al. 2018). The planetary candidate TOI-199.01, so named because it is the first transit signal detected in this light curve, is listed in the ExoFOP-TESS archive,[42] with a period of $P_{01} = 104.87075$ days. Prior to its release as a TOI, the WINE team had independently identified the initial single transit event in Sector 2 and begun follow-up observations.

Seven transits of the planetary candidate TOI-199.01 were observable for TESS, in Sectors 2, 10, 13, 29, 32, and 35. Numbering the first observed transit in Sector 2 as transit 1, these correspond to transits 1, 3, 4, 8, 9, 10, and 17 (note that transit 2 fell in the data gap between Sectors 5 and 6), respectively.

Unfortunately, one of the transits, close to the start of Sector 10, is cut off by quality checks in the 2 minute cadence Presearch Data Conditioning (PDCSAP; Stumpe et al. 2012, 2014; Smith et al. 2012) light curve, and another at the

[38] Located at https://exoplanetarchive.ipac.caltech.edu.
[39] Available at https://www.astro.keele.ac.uk/jkt/tepcat/. Accessed 2022 October 06.
[40] According to the NASA Exoplanet Archive, last accessed 2023 February 06.
[41] As of 2023 February 06, according to the NASA Exoplanet Archive.
[42] Located at https://exofop.ipac.caltech.edu/tess/target.php?id=309792357.

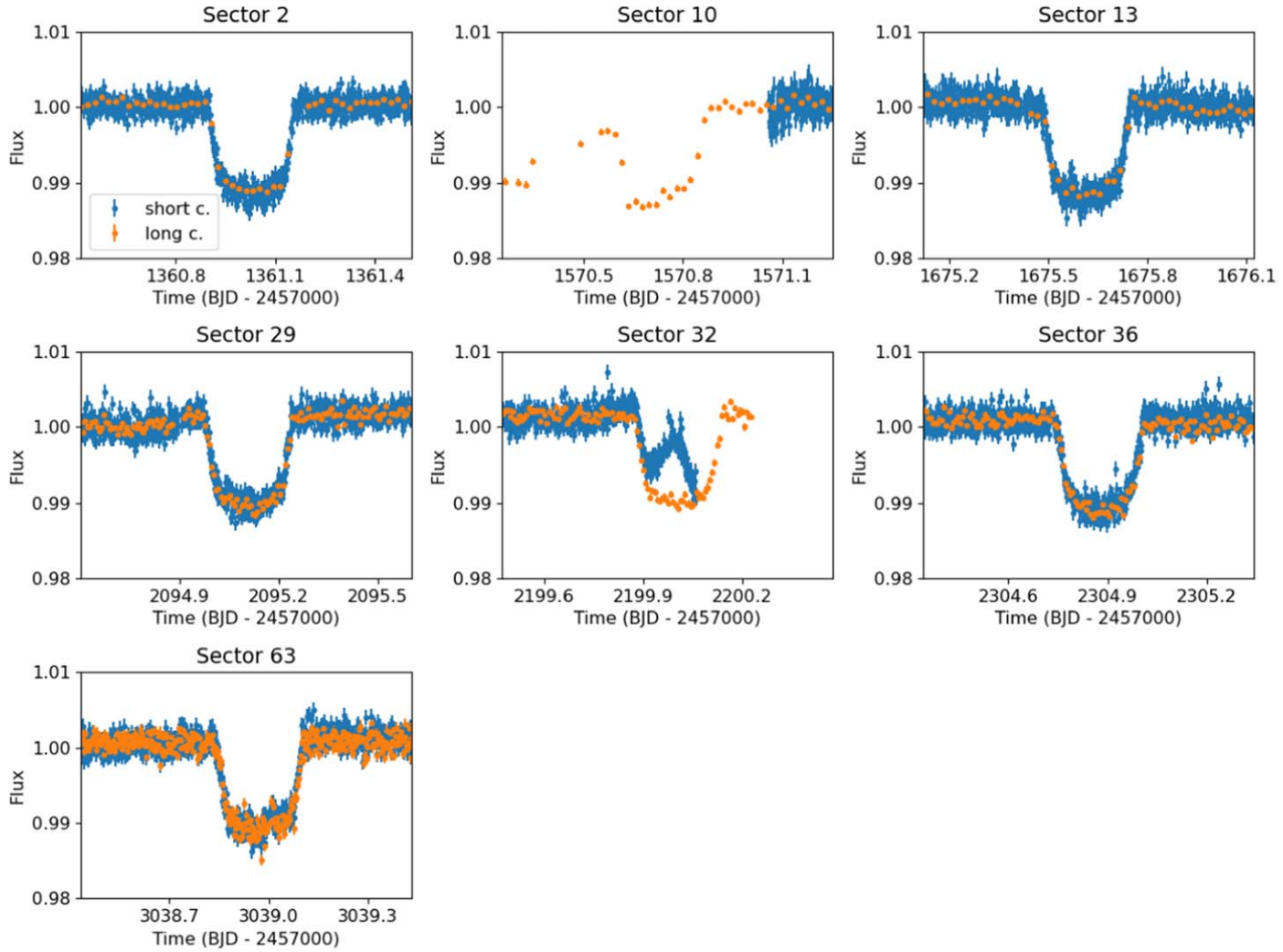

Figure 1. TESS light curves for TOI-199, for the seven sectors with transits. The short-cadence PDCSAP light curves are shown in blue, and the FFI light curves extracted with `tesseract` in orange. For Sectors 10 and 32 the transits could not be correctly recovered from the PDCSAP light curves.

end of Sector 32 is distorted. However, both are clearly seen in the light curves obtained from the Full Frame Images (FFIs), which we extracted with our own `tesseract` pipeline (F. Rojas et al. (2023, in preparation).[43] We attempted to rereduce the 2 minute cadence data to recover them, but were unable to retrieve the transit at the edge of Sector 10, where the light curve drops off sharply. Therefore, we chose to use the FFI light curves from `tesseract` for the whole of our analysis. The PDCSAP and FFI light curves for the seven sectors with transits are shown in Figure 1; note that the cadence for the FFIs changed from 30 minutes for the prime mission (top row) to 10 minutes for the first extended mission (middle row), and to 200 s for the second extended mission (bottom row).

2.2. Follow-up Photometry

At 21″ pixel^{-1}, the TESS pixels are relatively large, meaning that nearby companions can contaminate its photometry. Follow-up photometry is used to identify such cases of false positives, and to monitor transits not observed by TESS. TOI-199 was observed by five facilities, described in the following subsections.

[43] Publicly available at https://github.com/astrofelipe/tesseract.

2.2.1. ASTEP

Antarctica Search for Transiting ExoPlanets (ASTEP; Guillot et al. 2015; Mékarnia et al. 2016) is a 0.4 m telescope equipped with a Wynne Newtonian coma corrector, located on the East Antarctic Plateau. Until 2021 December it was equipped with a 4k × 4k front-illuminated FLI Proline KAF-16801E CCD with an image scale of 0.″93 pixel^{-1} resulting in a 1° × 1° corrected field of view. The focal instrument dichroic plate split the beam into a blue wavelength channel for guiding, and an unfiltered red science channel roughly matching the *Rc* transmission curve (Abe et al. 2013).

In 2022 January, the focal box was replaced with a new one with two high sensitivity cameras including an Andor iKon−L 936 at red wavelengths. The image scale is 1.″39 pixel^{-1} with a transmission curve centered on 850 ± 138 nm (Schmider et al. 2022).

The telescope is automated or remotely operated when needed. Due to the extremely low data transmission rate at the Concordia Station, the data are processed on site using IDL (Mékarnia et al. 2016) and Python (Dransfield et al. 2022) aperture photometry pipelines.

Three observations of TOI-199 were made with ASTEP, all of them with clear sky, winds between 3 and 5 m s^{-1}, and

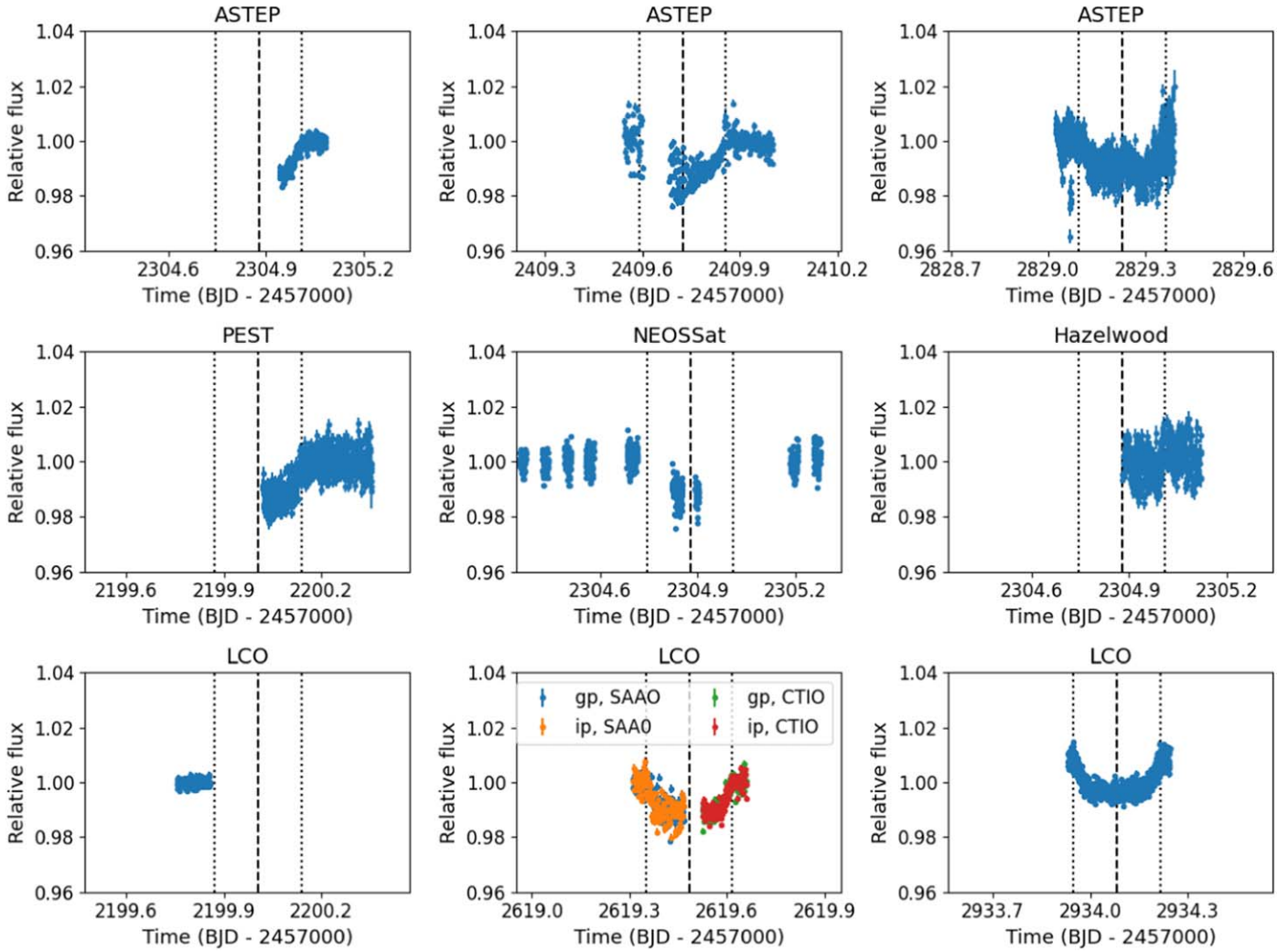

Figure 2. Follow-up photometry for TOI-199. Top row: light curves of ASTEP observations—an egress on 2021 March 31 (left), a full transit on 2021 July 13 (center), and a full transit on 2022 September 06 (right). Middle Row: light curves for PEST (left, egress on 2020 December 16), NEOSSat (center, full transit on 2021 March 31), and Hazelwood (right, egress on 2021 March 31) observations. Bottom row: light curves of LCO observations—a preingress flat curve on 2020 December 16 (left), two ingresses and egresses on 2022 February 08 (center), for which the points are color coded by filter and site, and a full transit on 2022 December 20 (right). In all panels, the dashed vertical line indicates the transit midpoint, and the dotted vertical lines the egress and ingress.

temperature ranging between $-62°$ and $-69°$C. An egress was observed on 2021 March 31 with an FWHM of $4\farcs3$, corresponding to the transit observed by TESS in Sector 36. Full transits were observed on 2021 July 13 and 2022 September 06 with FWHMs of $4\farcs3$ and $5\farcs9$, respectively, which were not observed by TESS. The Moon, 80% illuminated, was present during the 2021 March 31 and 2022 September 06 observations. The light curves are shown in Figure 2 (top row).

2.2.2. PEST

The Perth Exoplanet Survey Telescope (PEST) is a backyard observatory in Perth, Australia, operated by Thiam-Guan Tan. PEST was used to observe a transit egress of TOI-199.01 on 2021 December 16, corresponding to the transit observed by TESS in Sector 32. The observation was conducted with an *Rc* filter and 30 s integration times. At the time, the 0.3 m telescope was equipped with a 1530×1020 SBIG ST-8XME camera with an image scale of $1\farcs2$ pixel^{-1} resulting in a $31' \times 21'$ field of view. A custom pipeline based on C-Munipack was used to calibrate the images and extract the differential photometry using an aperture with radius $8\farcs6$. The light curve is shown in Figure 2 (middle row, left panel).

2.2.3. NEOSSat

The Near Earth Object Surveillance Satellite (NEOSSat; Laurin et al. 2008) is a Canadian microsatellite with a 0.15 m F/6 telescope which has a $0\fdg86 \times 0\fdg86$ field of view. Although designed for detecting and tracking near-Sun asteroids, it is also suitable for transit observations of bright stars (Fox & Wiegert 2022). NEOSSat observed a full transit of TOI-199.01 on 2021 March 31 with no filter, corresponding to the one observed by TESS in Sector 36. The light curve is shown in Figure 2 (middle row, center panel).

2.2.4. Hazelwood

The Hazelwood Observatory is a backyard observatory operated by Chris Stockdale in Victoria, Australia, with a 0.32 m Planewave CDK telescope working at f/8, a SBIG STT3200 2.2k × 1.5k CCD, giving a $20' \times 13'$ field of view and $0\farcs55$ pixel^{-1}. The camera is equipped with

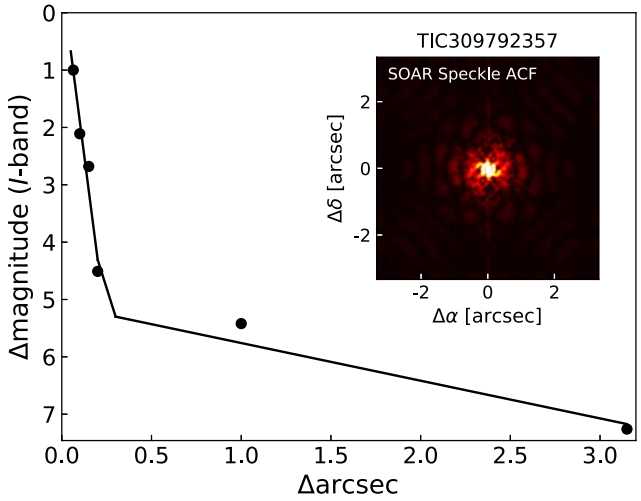

Figure 3. Contrast curve and speckle auto-correlation function from the HRCam at SOAR for TOI-199. The black points and solid line indicate the 5σ contrast curve; the inset shows the speckle auto-correlation function. No nearby sources are detected.

B, *V*, *Rc*, *Ic*, g', r', i' and z' filters (Astrodon Interference). The typical FWHM is $2\farcs2$ to $3\farcs0$. The Hazelwood Observatory observed an egress of TOI-199.01 in *Rc* on 2021 March 31, corresponding to the transit observed by TESS in Sector 36. Time series images were collected, bias, dark, and flat fielded and the transit analyzed with `AstroImageJ` (Collins et al. 2017). The reduced data were then uploaded to ExoFOP. The light curve is shown in Figure 2 (middle row, right panel).

2.2.5. LCO

The Las Cumbres Observatory Global Telescope network (LCOGT; Brown et al. 2013) is a globally distributed network of telescopes. The 1 m telescopes are equipped with 4096×4096 SINISTRO cameras having an image scale of $0\farcs389$ pixel^{-1}, resulting in a $26' \times 26'$ field of view. LCO observed TOI-199 several times with the Sinistro instrument: a preingress flat curve on 2021 December 16, corresponding to the transit observed by TESS in Sector 32, from the Cerro Tololo Inter-American Observatory (CTIO) site in the *zs* filter; an ingress on 2022 February 08, from the South African Astronomical Observatory (SAAO) site, in alternating *gp* and *ip* filters; the egress of the same transit, from the CTIO site, also in alternating *gp* and *ip* filters; and a full transit on 2022 December 20, from the Siding Springs Observatory (SSO) site. The images were calibrated by the standard LCOGT `BANZAI` pipeline (McCully et al. 2018), and photometric data were extracted using `AstroImageJ`. The light curves are shown in Figure 2 (bottom row).

2.3. High-resolution Imaging

Given the relatively large pixel size of TESS, high-resolution imaging from the ground is a valuable tool to assess possible blends and contamination from nearby sources. The SOAR TESS survey (Ziegler et al. 2020) observes TESS exoplanet candidate hosts with speckle imaging using the high-resolution camera (HRCam) imager on the 4.1 m Southern Astrophysical Research (SOAR) telescope at Cerro Pachón, Chile (Tokovinin 2018), in order to detect such nearby sources. TOI-199 was observed on the night of 2019 February 18, with no nearby sources detected within $3''$. The contrast curve and speckle auto-correlation function are shown in Figure 3.

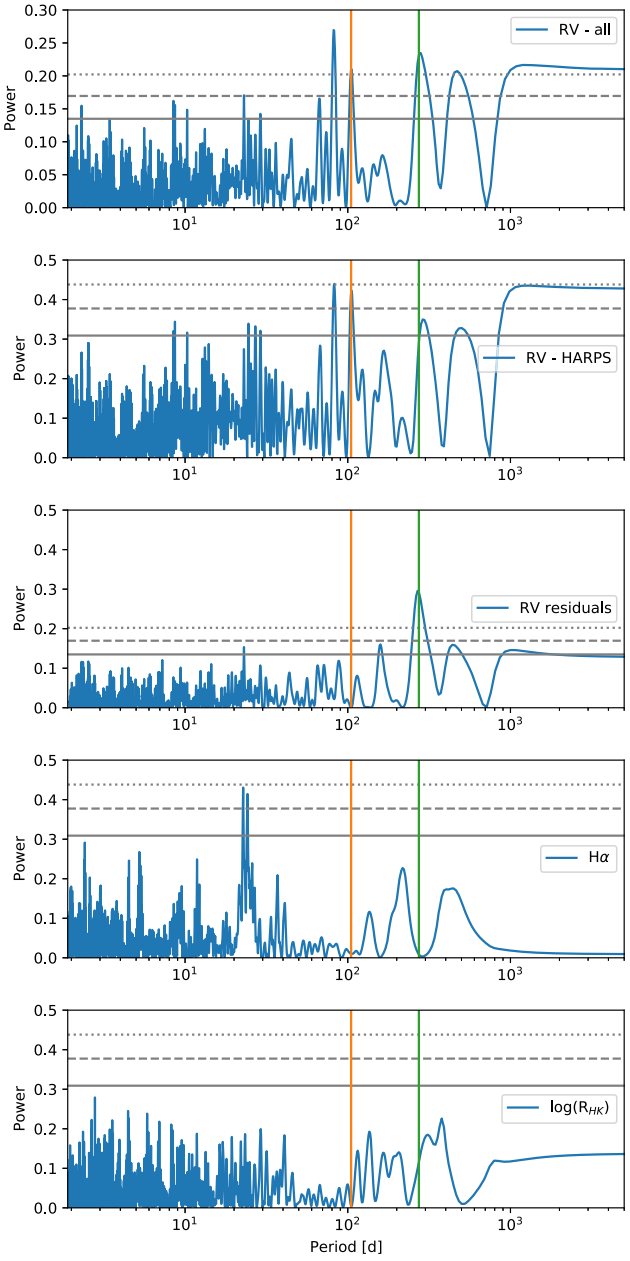

Figure 4. Periodograms of the joint RVs (top panel); the HARPS RVs alone (second panel); the joint RV residuals to a one-planet fit for TOI-199 b (third panel); the HARPS Hα indicator (fourth panel); and the HARPS $\log(R'_{\rm HK})$ activity indicator (bottom panel). The gray solid, dashed, and dotted horizontal lines indicate false alarm probability levels of 10%, 1%, and 0.1%, respectively. The periods of the two planets are indicated with vertical orange and green lines. We note that the peak at ~81 days is a one year alias of the ~104 day planet.

2.4. Spectroscopic Data

The WINE consortium carried out spectroscopic follow up of TOI-199 with the HARPS, FEROS, CORALIE, and CHIRON spectrographs. We also received additional CORALIE and CHIRON RVs from other teams, which we incorporated into the analysis. All the resulting RVs are shown in Figure 12 (top panel). Figure 4 shows the GLS periodograms of the joint RVs from all four spectrographs (top panel); of the

HARPS RVs alone (second panel); of the joint RV residuals to a fit of the inner planet alone (third panel); and of the Hα and $\log(R'_{\rm HK})$ activity indicators computed from the HARPS spectra (fourth and fifth panels).

2.4.1. HARPS

We observed TOI-199 with the HARPS spectrograph (Mayor et al. 2003) at the 3.6 m telescope at La Silla, with resolving power $R = 120{,}000$, between 2018 December 12 and 2021 March 09. We obtained 46 spectra, under Program IDs 0101.C-0510, 0102.C-0451, 0104.C-0413, and 106.21ER.001. For the first three programs (2018 December through 2020 February), we operated in simultaneous sky mode, obtaining 26 spectra with 900 s exposure durations. For the last (2020 December through 2021 March), we switched to simultaneous Fabry–Perot mode as part of an overall revision of our observing program, obtaining 20 spectra with an increased 1200 s exposure duration. The spectra have a median signal-to-noise ratio (S/N) of 62. We processed the spectra using the `CERES` pipeline (Brahm et al. 2017a), which provides both RVs and several activity indicators: the CCF bisector (BIS; e.g., Queloz et al. 2001a), and the Hα (Boisse et al. 2009), $\log(R'_{\rm HK})$ (Duncan et al. 1991; Noyes et al. 1984), Na II, and He I (Gomes da Silva et al. 2011) activity indices. The resulting RVs and activity indicators are listed in Table A1; the RVs have a median error of 2.4 m s^{-1}.

2.4.2. FEROS

We observed TOI-199 with the FEROS spectrograph (Kaufer et al. 1999) at the MPG 2.2 m telescope at La Silla, with resolving power $R = 50{,}000$, between 2018 November 27 and 2020 March 04. We obtained 48 spectra, under Program IDs 0102.A-9003, 0102.A-9006, 0102.A-9011, 0102.A-9029, 0103.A-9008, and 0104.A-9007 in object-calibration mode, with 500 s exposure durations (save three spectra with increased exposure times due to poor observing conditions, two of 700 s and one of 1000s). The spectra have a median S/N of 90. As with the HARPS data, we processed the spectra using the `CERES` pipeline. The resulting RVs and activity indicators are listed in Table A2; the RVs have a median error of 6.3 m s^{-1}.

2.4.3. CORALIE

TOI-199 was observed with the CORALIE spectrograph (Queloz et al. 2001b) at the Swiss 1.2 m Euler telescope at La Silla by both the WINE and Swiss teams. In total, 19 spectra were obtained between 2018 December 27 and 2019 December 02, with a median exposure duration of 1200 s. CORALIE is a fiber-fed echelle spectrograph with a 2″ science fiber, and a secondary fiber with a Fabry–Perot for simultaneous wavelength calibration. It has a spectral resolution of $R = 60{,}000$. RVs are extracted using the standard CORALIE DRS by cross-correlating the spectra with a binary G2V template (Baranne et al. 1996; Pepe et al. 2002). The BIS, FWHM, and other line-profile diagnostics were also computed via the CORALIE DRS, as was the Hα index for each spectrum to check for possible variation in stellar activity. The resulting RVs and activity indicators are listed in Table A3; the RVs have a median error of 13.7 m s^{-1}.

2.4.4. CHIRON

TOI-199 was observed with the CHIRON spectrograph (Tokovinin et al. 2013) at the SMARTS 1.5 m telescope at CTIO by both the WINE team and Dr Carleo. In total, 26 spectra were obtained between 2019 March 11 and 2020 December 13; the WINE team observed with single 1500 s exposures, while Dr Carleo observed sets of three 600 s exposures. RVs were extracted following Jones et al. (2019). The resulting RVs and activity indicators are listed in table A4; the RVs have a median error of 11.3 m s^{-1}.

3. Analysis

3.1. Stellar parameters

We use a two-part process to characterize the host star. First, we employed the coadded FEROS spectra to determine the atmospheric parameters of TOI-199. To do this, we used the `ZASPE` code (Brahm et al. 2017b), which compares the observed spectrum to a grid of synthetic models (generated from ATLAS9 model atmospheres; Castelli & Kurucz 2003) in order to determine the effective temperature $T_{\rm eff}$, surface gravity $\log g$, metallicity [Fe/H], and projected rotational velocity $v \sin i$.

Second, we followed the second procedure described in Brahm et al. (2019) to determine the physical parameters of the host star. To summarize, we compare the broadband photometric measurements (converted to absolute magnitudes via the Gaia DR3 parallax; Gaia Collaboration et al. 2016, 2022) with the stellar evolutionary models of Bressan et al. (2012). We use the `emcee` package (Foreman-Mackey et al. 2013) to sample the posterior distributions. Through this procedure, we determine the age, mass, radius, luminosity, density, and extinction. This also enables us to compute new values for $T_{\rm eff}$ and $\log g$, the latter of which is more precise than the one previously determined through `ZASPE`. Therefore, we iterate the entire procedure, using the new $\log g$ as an additional input parameter for `ZASPE`. One iteration was sufficient for the $\log g$ value to converge.

The final stellar parameters computed, and other observational properties of TOI-199 are presented in Table 1. We find that TOI-199 is a late G-type star. The quoted error bars for the stellar parameters are internal errors, computed as the $\pm 1\sigma$ interval around the median of the posterior for each parameter; they do not take into account systematic errors in the stellar models.

Recently, Tayar et al. (2022) examined the uncertainty floors on fundamental stellar parameters. Specifically, they find fundamental floors of 2.4% for $T_{\rm eff}$, 2% for $L_\star$, and 4.2% for $R_\star$ due to the uncertainties on input observables such as the bolometric flux and angular diameter. We also report these values in Table 1. For $M_\star$ and the stellar age, they perform a comparison between four model grids. We use the online interface provided to carry out the same comparison for TOI-199, and report the standard deviation of the resulting values in Table 1.

3.2. TTV Extraction

We used the `juliet`[44] software (Espinoza et al. 2019) to extract the TTVs. We focused on the TESS, ASTEP, and LCO

[44] Available at https://github.com/nespinoza/juliet.

Table 1
Stellar Parameters of TOI-199

Parameter	Value	Reference
Names	CD-60 1144	
	TIC309792357, TOI-199	TESS
	J05202531-5953443	2MASS
	4762582895440787712	Gaia DR3
R.A. (J2000)	$05^{h}20^{m}25\overset{s}{.}3151633088$	Gaia DR3
Decl. (J2000)	$-59°53'44\overset{''}{.}463213656$	Gaia DR3
$pm^{R.A.}$ [mas yr^{-1}]	45.864	Gaia DR3
$pm^{Decl.}$ [mas yr^{-1}]	58.445	Gaia DR3
π [mas]	9.8296	Gaia DR3
T [mag]	10.0391	TESS
B [mag]	11.59	Tycho2
V [mag]	10.70	Tycho2
J [mag]	9.329	2MASS
H [mag]	8.952	2MASS
K [mag]	8.814	2MASS
$T_{\rm eff}$[K]	5255^{+12}_{-10} (126)	This work
Spectral type	G9V	PM13
Fe/H [dex]	0.22 ± 0.03	This work
$\log g$ [dex]	$4.582^{0.003}_{-0.006}$	This work
$v \sin i$ [km s^{-1}]	0.5 ± 0.6	This work
$R_\star$ [$R_\odot$]	0.820 ± 0.003 (0.03)	This work
$M_\star$ [$M_\odot$]	$0.936^{+0.003}_{-0.005}$ (0.009)	This work
$L_\star$ [$L_\odot$]	$0.459^{+0.005}_{-0.003}$ (0.009)	This work
$\rho_\star$ [g cm^{-3}]	$2.39^{+0.02}_{-0.04}$	This work
Age [Gyr]	$0.8^{+1.2}_{-0.6}$ (0.72)	This work
A_V [mag]	$0.01^{+0.02}_{-0.01}$	This work
$\log R'_{\rm hk}$	-4.77 ± 0.13	This work

Note. TESS: TESS Input Catalog (Stassun 2019); 2MASS: Two-micron All Sky Survey (Skrutskie et al. 2006); Gaia DR3: Gaia Data Release 3 (Gaia Collaboration et al. 2016, 2022); Tycho2: the Tycho-2 Catalogue (Høg et al. 2000); and PM13: using the tables of Pecaut & Mamajek (2013). Values in parentheses correspond to the fundamental uncertainty floors following Tayar et al. (2022).

Table 2
Prior and Posterior Planetary Parameter Distributions for the TTV Extraction with `juliet`

Parameter	Prior[a]	Posterior
p_b	$\mathcal{N}(0.1023, 0.00915)$	0.1015 ± 0.0005
b_b	$\mathcal{N}(0.47, 0.555)$	$0.45^{+0.02}_{-0.03}$
e_b	0.0 (fixed)	0.0 (fixed)
ω_b	90.0 (fixed)	90.0 (fixed)
ρ	$\mathcal{J}(100.0, 10{,}000.0)$	3431^{+160}_{-140}
$T_{b,\rm TESS,\ 2}$	$\mathcal{U}(2{,}458{,}360.89, 2{,}458{,}361.14)$	$2{,}458{,}361.0283 \pm 0.0008$
$T_{b,\rm TESS,\ 10}$	$\mathcal{U}(2{,}458{,}570.63, 2{,}458{,}570.88)$	$2{,}458{,}570.732 \pm 0.001$
$T_{b,\rm TESS,\ 13}$	$\mathcal{U}(2{,}458{,}675.50, 2{,}458{,}675.75)$	$2{,}458{,}675.6182 \pm 0.0009$
$T_{b,\rm TESS,\ 29}$	$\mathcal{U}(2{,}459{,}094.98, 2{,}459{,}095.23)$	$2{,}459{,}095.1087^{+0.0010}_{-0.0009}$
$T_{b,\rm TESS,\ 32}$	$\mathcal{U}(2{,}459{,}199.85, 2{,}459{,}200.10)$	$2{,}459{,}200.0050 \pm 0.0006$
$T_{b,\rm TESS,\ 36}$	$\mathcal{U}(2{,}459{,}304.72, 2{,}459{,}304.97)$	$2{,}459{,}304.8770^{+0.0009}_{-0.0010}$
$T_{b,\rm TESS,\ 63}$	$\mathcal{U}(2{,}460{,}038.81, 2{,}460{,}039.06)$	$2{,}460{,}038.9735 \pm 0.0004$
$T_{b,\rm ASTEP,\ 1}$	$\mathcal{U}(2{,}459{,}304.72, 2{,}459{,}304.97)$	$2{,}459{,}304.8774 \pm 0.0008$
$T_{b,\rm ASTEP,2}$	$\mathcal{U}(2{,}459{,}409.59, 2{,}459{,}409.84)$	$2{,}459{,}409.7229 \pm 0.0007$
$T_{b,\rm ASTEP,3}$	$\mathcal{U}(2{,}459{,}829.07, 2{,}459{,}829.32)$	$2{,}459{,}829.2283 \pm 0.0005$
$T_{b,\rm PEST}$	$\mathcal{U}(2{,}459{,}199.85, 2{,}459{,}200.10)$	$2{,}459{,}200.019 \pm 0.001$
$T_{b,\rm NEOSSat}$	$\mathcal{U}(2{,}459{,}304.72, 2{,}459{,}304.97)$	$2{,}459{,}304.900^{+0.002}_{-0.003}$
$T_{b,\rm Hwd}$	$\mathcal{U}(2{,}459{,}304.72, 2{,}459{,}304.97)$	$2{,}459{,}304.759 \pm 0.002$
$T_{b,\rm LCO,1}$	$\mathcal{U}(2{,}459{,}199.85, 2{,}459{,}200.10)$	$2{,}459{,}200.04 \pm 0.03$
$T_{b,\rm LCO,2}$	$\mathcal{U}(2{,}459{,}619.33, 2{,}459{,}619.58)$	$2{,}459{,}619.482 \pm 0.002$
$T_{b,\rm LCO,3}$	$\mathcal{U}(2{,}459{,}619.33, 2{,}459{,}619.58)$	$2{,}459{,}619.480 \pm 0.001$
$T_{b,\rm LCO,4}$	$\mathcal{U}(2{,}459{,}619.33, 2{,}459{,}619.58)$	$2{,}459{,}619.486 \pm 0.001$
$T_{b,\rm LCO,5}$	$\mathcal{U}(2{,}459{,}619.33, 2{,}459{,}619.58)$	$2{,}459{,}619.485 \pm 0.001$
$T_{b,\rm LCO,6}$	$\mathcal{U}(2{,}459{,}933.94, 2{,}459{,}934.19)$	$2{,}459{,}934.0818 \pm 0.0003$
P_b[b] [day]	–	104.87236 ± 0.00005
a_b [au]	–	$0.480^{+0.007}_{-0.008}$
$T0_b$[b] [BJD]	–	$2{,}458{,}256.1286 \pm 0.0006$
R_b [R_J]	–	0.810 ± 0.005
i_b [deg]	–	89.81 ± 0.02

Notes. Top: fitted parameters. Bottom: derived orbital parameters and physical parameters.
[a] $\mathcal{U}(a, b)$ indicates a uniform distribution between a and b; $\mathcal{N}(a, b)$ a normal distribution with mean a and standard deviation b; $\mathcal{J}(a, b)$ a Jeffreys or log-uniform distribution between a and b.
[b] `juliet` computes the P and T0 in a TTV fit as the slope and intercept, respectively, of a least-squares fit to the transit times. We adopt the value from the full TTV+RV model (Section 3.3) as our final period.

transits, as the second and third ASTEP transits and second and third LCO transits are the only ones not also observed by TESS. The other light curves are consistent with the TESS observations, as shown in Figures 8 and 9.

The `tesseract` FFI light curves are uncorrected for systematics and other effects. We used a two-step method to fit a Gaussian process (GP) to each TESS sector, first optimizing the hyperparameters on the out-of-transit data, with broad priors of $\mathcal{J}(10^{-6}, 10^{6})$ for $\sigma_{\rm GP,\ TESS,\ i}$, where $\mathcal{J}(a, b)$ is a Jeffreys or log-uniform distribution between a and b, and $\mathcal{J}(10^{-3}, 10^{3})$ for $\rho_{\rm GP,\ TESS,\ i}$ for each TESS sector i. We then used the resulting posterior parameters as priors on the GP hyperparameters in the full fit including the transits, adopting the upper and lower 1σ bounds from the posteriors as limits on new Jeffreys distributions. Each transit is fit independently, with individual priors for the flux offsets $m_{\rm flux,instrument,transit}$ and jitters $\sigma_{\rm instrument,transit}$. `juliet` also requires priors for the dilution factors $m_{\rm d,instrument,transit}$, which we have fixed to 1 for all instruments and transits. The limb-darkening parameters $q_{1,\rm instrument}$ and $q_{2,\rm instrument}$ are common to all transits observed with each instrument (save for LCO, where the observations were made at different sites or/and with different filters). For each $q_{\rm i,instrument}$ we adopted truncated normal priors, where the mean of each prior was based on the derivation of limiting quadratic coefficients from the nonlinear coefficients described by Espinoza & Jordán (2015).[45] We used ATLAS model atmospheres interpolated over 100 μ-points, as in Claret & Bloemen (2011), and instrument response functions from the instrument website (for LCO, which provides profiles for all available filters) or from the SVO Filter Profile Service (Rodrigo et al. 2012; Rodrigo & Solano 2020; for TESS there is a specific profile; we adopted a generic Johnson V filter profile for NEOSSat, which observed without a filter, and a Cousins R filter for the rest of the instruments, which observed with R filters). For the transit times $T_{b,\rm instrument,transit}$, we adopt uniform priors with a width of 6 hr, and midpoints determined from the orbital period listed in ExoFOP. The ExoFOP values for the planet-to-star radius ratio p_b and the impact parameter b_b were also used as priors. The eccentricity e_b and ω_b were fixed to 0° and 90°, respectively. While we may expect planets at

[45] As implemented in the public repository https://github.com/nespinoza/limb-darkening.

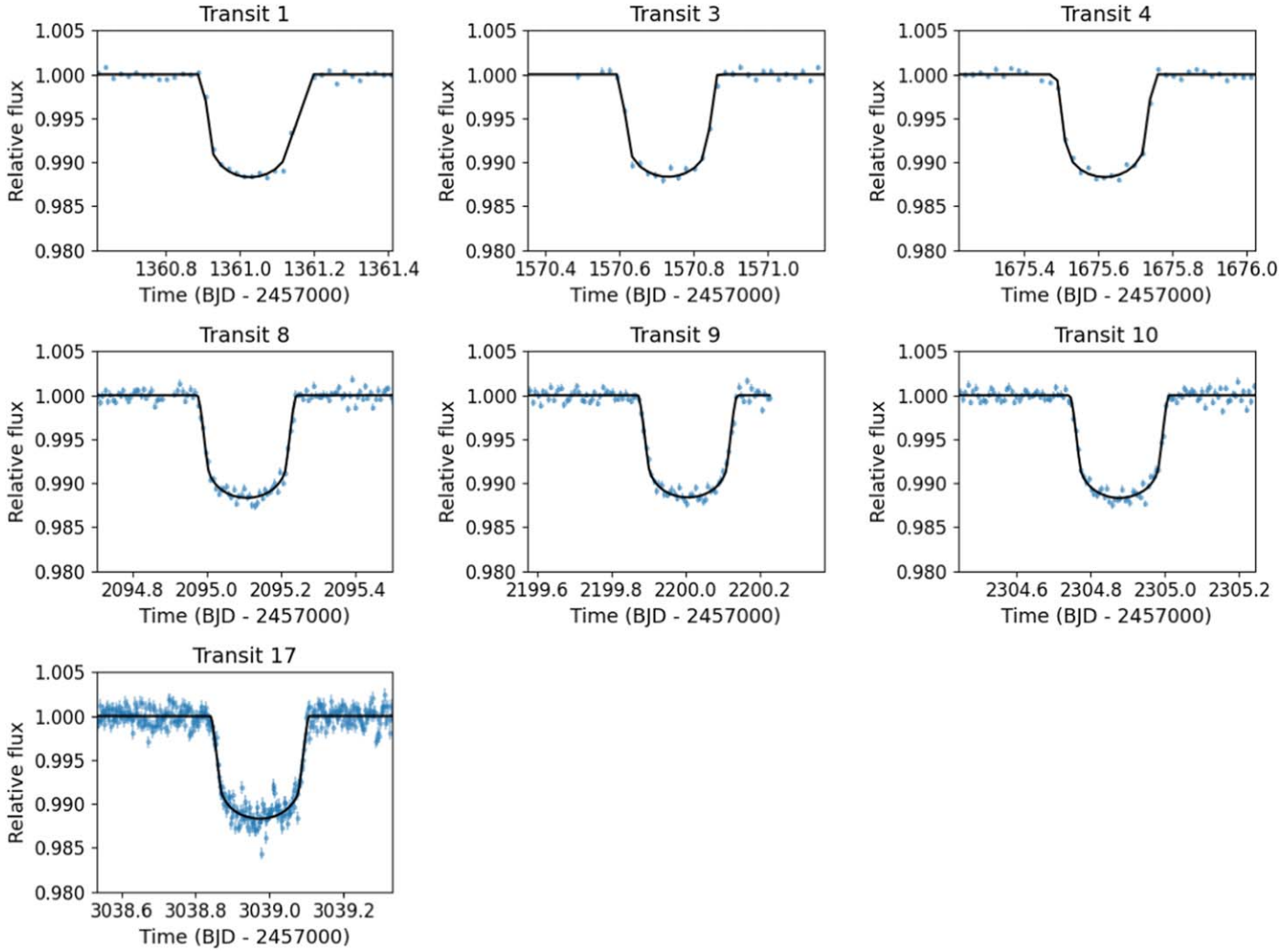

Figure 5. TESS FFI light curves, extracted with `tesseract` (blue points), and fitted models (black lines) for the seven transits observed with TESS. The GP components of each model have been subtracted.

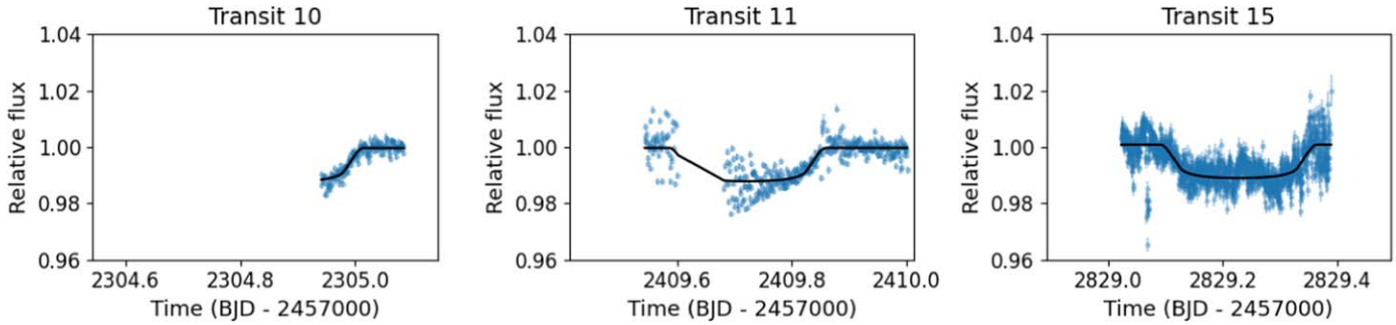

Figure 6. ASTEP light curves (blue points) and fitted models (black lines) for the three transits observed with ASTEP.

∼100 days to have noncircular orbits, the shape of the transit will be noticeably altered only for large eccentricities, so a fixed eccentricity suffices for the TTV extraction (we note the eccentricity is a free parameter in the full RV+TTV model, see Section 3.3). The priors and posteriors for the full fit are listed in Table 2 for the planetary parameters, and in Table B1 for the instrumental and GP parameters. The fitted TESS, ASTEP, and LCO transits are shown in Figures 5, 6, and 7, respectively, and the O – C plot is shown in Figure 10.

3.3. Joint TTV and RV Model

We used the `Exo-Striker`[46] software (Trifonov 2019) to jointly fit the RV and the TTV data of TOI-199. We use a very similar approach to the TTV+RV *N*-body modeling scheme analysis done for the TOI-2202 system in Trifonov et al. (2021); we refer to this paper for more details on the TTV+RV

[46] Available at https://github.com/3fon3fonov/exostriker.

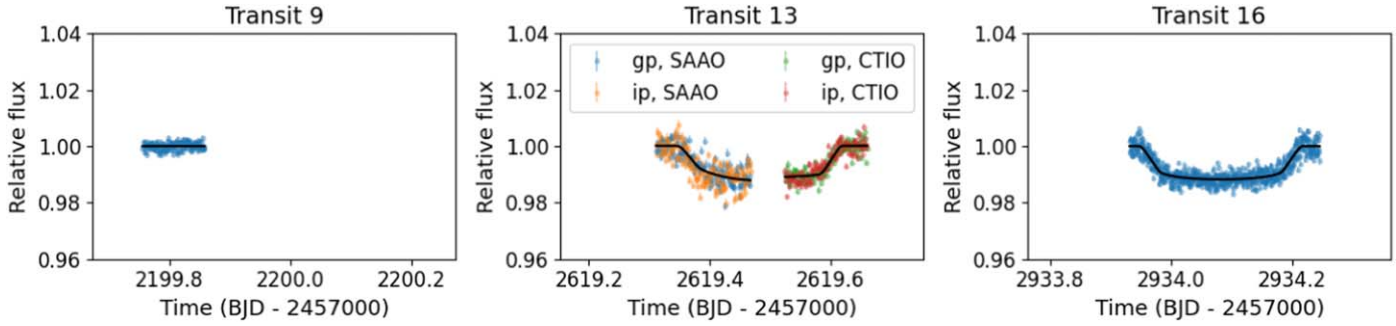

Figure 7. LCO light curves (colored points) and fitted models (black lines) for the three transits observed with LCO. The data for transit 13 are colored by filter and site, as in Figure 2.

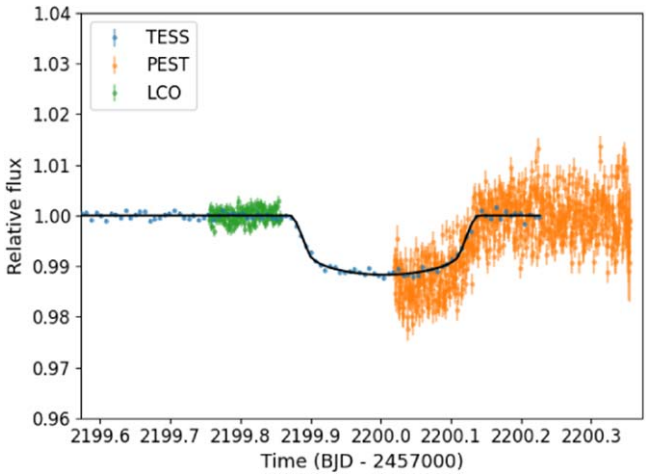

Figure 8. TESS FFI light curve for Sector 32 extracted with `tesseract` (blue points), PEST light curve (orange points), LCO light curve (green points), and fitted model to the TESS data (black line) for transit 9.

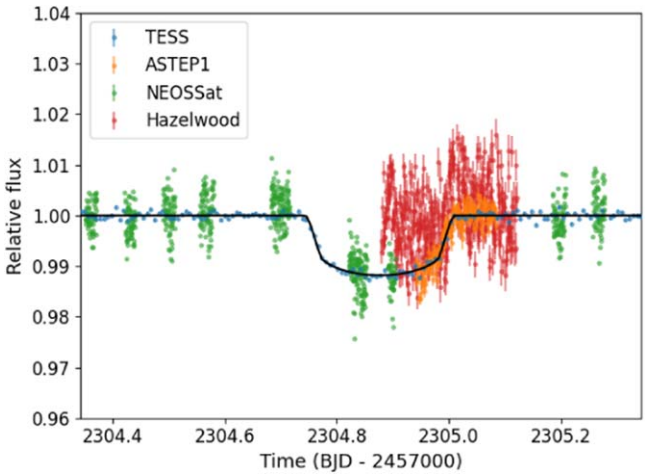

Figure 9. TESS FFI light curve for Sector 36 extracted with `tesseract` (blue points), ASTEP light curve (orange points), NEOSSat light curve (green points), Hazelwood light curve (red points), and fitted model to the TESS data (black line) for transit 10.

modeling scheme used here. Briefly, the *N*-body RV modeling used is native to `Exo-Striker`, whereas the TTV modeling uses the `TTVFast` package (Deck et al. 2014). The fitted parameters for each planet in our joint model are the semiamplitude K, the orbital period P, eccentricity e, argument of periastron ω, and mean-anomaly M_0. For our fitting analysis, we assumed a coplanar, edge-on, and prograde two-planet system (i.e., i_b, $i_c = 90°$ and $\Delta i = 0°$), and for the stellar mass of TOI-199 we adopt our best estimate of $0.936^{+0.003}_{-0.005}\ M_\odot$ (note that the stellar mass uncertainties are not included in the modeling, but are incorporated into the final uncertainties of the derived planetary parameters). The time step in the dynamical model was set to 1 day, assuring adequate model precision. Additionally, we optimize two parameters for each Doppler data set, the offset and the RV "jitter." This latter parameter is added in quadrature to the nominal uncertainties of the RV data (Baluev 2009).

We constructed parameter posteriors by the nested sampling algorithm (Skilling 2004), implemented via the `dynesty` package (Speagle 2020). For TOI-199 b, we used the previous light-curve characterization with `juliet` and the RV period search results to constrain the priors on the parameters. For the period of the perturber, we first ran initial joint fits with broad priors in P_c between 150 and 330 days, e_c between 0 and 0.4, and ω_c and $M0_c$ between 0° and 360° covering first- and second-order mean-motion resonance (MMR) period ratios. From these, we could constrain the orbital period to a range of 265–290 days for the final fits.

We tested three models: two planets, two planets plus a linear trend, and two planets plus a quadratic trend. A visual hint of a long-term RV variation prompted the addition of trends. The comparison of the Bayesian likelihood factors favors the model with two planets and no trend ($\Delta \ln \mathcal{Z} = 15$ between the no-trend and quadratic-trend models). Therefore, we adopted the model with two planets and no additional trends, although we intend to continue monitoring this system for potential long-term RV variations that could point to the existence of more distant companions. The arguments of pericenter ω_b and ω_c required careful handling of the priors to avoid circular multimodality and ensure convergence within a reasonable time frame; we constrained them through preliminary fits. The final priors adopted are listed in Table 3.

The joint TTV and RV model results in TOI-199 b having a period of $104.854^{+0.001}_{-0.002}$ days, an eccentricity of $0.09^{+0.01}_{-0.02}$, a radius of $0.888 \pm 0.006\ R_J$, and a mass of $0.17 \pm 0.02\ M_J$. Meanwhile, TOI-199 c has a period of $273.69^{+0.26}_{-0.22}$ days, an eccentricity of $0.096^{+0.008}_{-0.009}$, and a minimum dynamical mass (since in the dynamical model we fix $i_c = 90°$) of $m_c = 0.28^{+0.02}_{-0.01}\ M_J$. If it were a transiting planet, TESS should have seen transits in Sectors 5 and 35, but the light curves are flat around the predicted times of transit. In Figure 11 we show the light curves together with model transits for the expected range

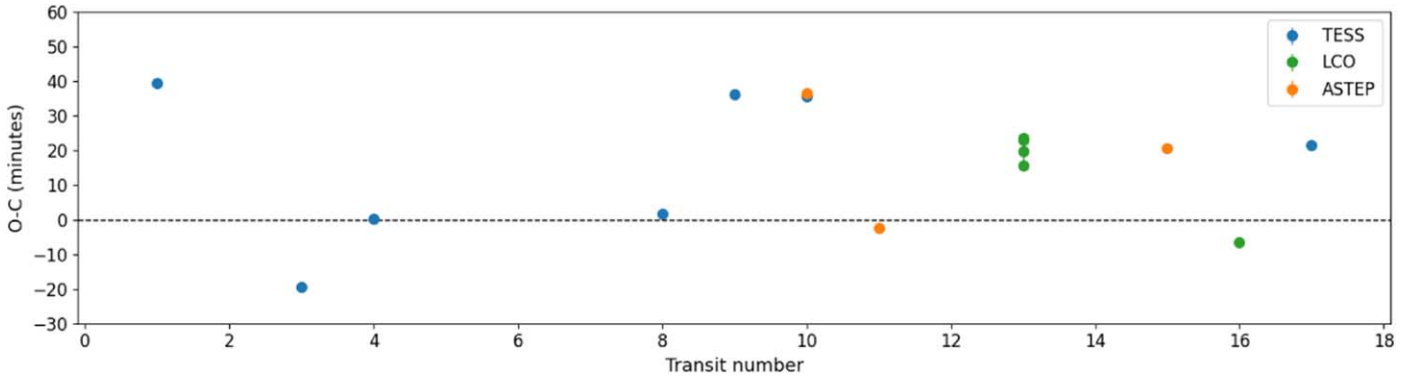

Figure 10. O – C plot (difference between predicted and observed transit midpoint times) for the TESS, ASTEP, and LCO transits. The error bars are generally smaller than the marker size.

Table 3
Prior and Posterior Parameter Distributions for the Joint TTV+RV Fit for the TOI-199 System Obtained with a Self-consistent *N*-body Model with `Exo-Striker` at Epoch BJD = 2,458,256.14

	Prior		Median & 1σ		Max $-\ln\mathcal{L}$	
Parameter	Planet b	Planet c	Planet b	Planet c	Planet b	Planet c
K [m s^{-1}]	$\mathcal{U}$[a](5, 20)	$\mathcal{U}$(3, 20)	7.7 ± 1.1	$9.1^{+0.5}_{-0.4}$	7.7	8.8
P [day]	$\mathcal{U}$(104.60, 105.00)	$\mathcal{U}$(265.00, 290.00)	$104.854^{+0.001}_{-0.002}$	$273.69^{+0.26}_{-0.22}$	104.855	273.55
e	$\mathcal{U}$(0, 0.4)	$\mathcal{U}$(0.0, 0.4)	$0.09^{+0.01}_{-0.02}$	$0.096^{+0.008}_{-0.009}$	0.102	0.107
ω [degrees]	$\mathcal{U}$(–30, 30)	$\mathcal{U}$(270, 450)	350^{+2}_{-4}	8^{+4}_{-7}[b]	351	11[b]
M_0 [degrees]	$\mathcal{U}$(45, 135)	$\mathcal{U}$(90, 270)	111 ± 2	192^{+4}_{-3}	110	190
a [au]	–	–	0.4254 ± 0.002	0.807 ± 0.003	0.4254	0.806
m[c] [$M_{\rm jup}$]	–	–	0.17 ± 0.02	$0.28^{+0.02}_{-0.01}$	0.17	0.27
RV$_{\rm off\ FEROS}$ [m s^{-1}]	$\mathcal{U}$(51,270, 51,370)		$51{,}326.7^{+2.9}_{-3.1}$		51,324.5	
RV$_{\rm off\ HARPS}$ [m s^{-1}]	$\mathcal{U}$(51,270, 51,370)		$51{,}350.4^{+1.0}_{-0.9}$		51,349.4	
RV$_{\rm off\ CHIRON}$ [m s^{-1}]	$\mathcal{U}$(–50, 10)		$-0.5^{+4.2}_{-3.9}$		−0.2	
RV$_{\rm off\ CORALIE}$ [m s^{-1}]	$\mathcal{U}$(51,270, 51,370)		$51{,}331.0^{+3.1}_{-3.3}$		51,327.1	
RV$_{\rm jit\ FEROS}$ [m s^{-1}]	$\mathcal{U}$(0.01, 40.00)		$19.9^{+2.6}_{-2.1}$		21.1	
RV$_{\rm jit\ HARPS}$ [m s^{-1}]	$\mathcal{U}$(0.01, 40.00)		$5.5^{+0.8}_{-0.6}$		5.1	
RV$_{\rm jit\ CHIRON}$ [m s^{-1}]	$\mathcal{U}$(0.01, 40.00)		$11.9^{+4.8}_{-3.7}$		14.9	
RV$_{\rm jit\ CORALIE}$ [m s^{-1}]	$\mathcal{U}$(0.01, 40.00)		$5.4^{+4.4}_{-3.5}$		4.3	

Notes. The given values and error bars correspond to the median and 1σ of the posterior distributions, respectively. Top: planetary parameters. Bottom: RV offsets and jitters.
[a] $\mathcal{U}(a, b)$ indicates a uniform distribution between a and b.
[b] 360° has been added to/subtracted from the median and max $-\ln\mathcal{L}$ values of ω_b and ω_c, respectively, to show the orbital alignment between the two planets better.
[c] Mass corresponding to an edge-on coplanar model.

of radii from interior models (Section 4.2) and impact parameters of $b = 0$ and $b = 0.75$, any of which should have been easily detectable in the TESS light curves. Given the stellar radius, the planet's semimajor axis, and its predicted radii, this sets an upper limit on its inclination of $i_c \lessapprox 89.7°$. Our model assumption that the system is edge on and coplanar (i.e., i_b, $i_c = 90°$, and $\Delta i = 0°$) is still reasonable, since large mutual inclinations are unlikely, whereas small deviations from an edge-on configuration will not lead to a significant discrepancy from the derived (minimum) dynamical masses.

The phase-folded RVs for TOI-199 b and c are shown in Figure 12 (bottom center and right panels, respectively), and the TTVs and fitted model in Figure 12, bottom left panel. The full list of posterior parameters is given in Table 3, and the posterior probability distribution plots are shown in Figures C1, C2, C3, and C4. The osculating orbital parameters, which

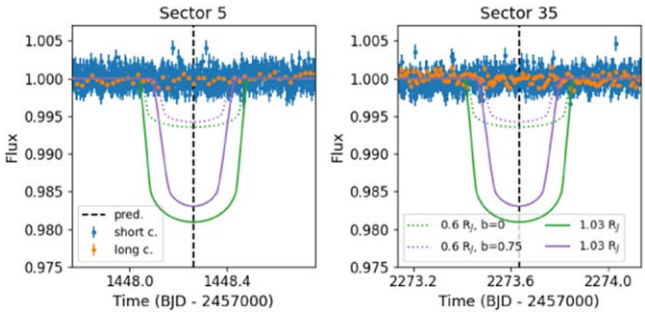

Figure 11. Predicted transits for TOI-199 c, which does not transit. Blue and orange points indicate the PDCSAP and `tesseract` light curves, respectively, as in Figure 1. The vertical dashed line indicates the expected time of midtransit. Model transits from `batman` are shown for two radii, $R_c = 1.03\ R_J$ (solid lines) and $R_c = 0.6\ R_J$ (dotted lines), and for two impact parameters, $b = 0$ (green) and $b = 0.75$ (purple).

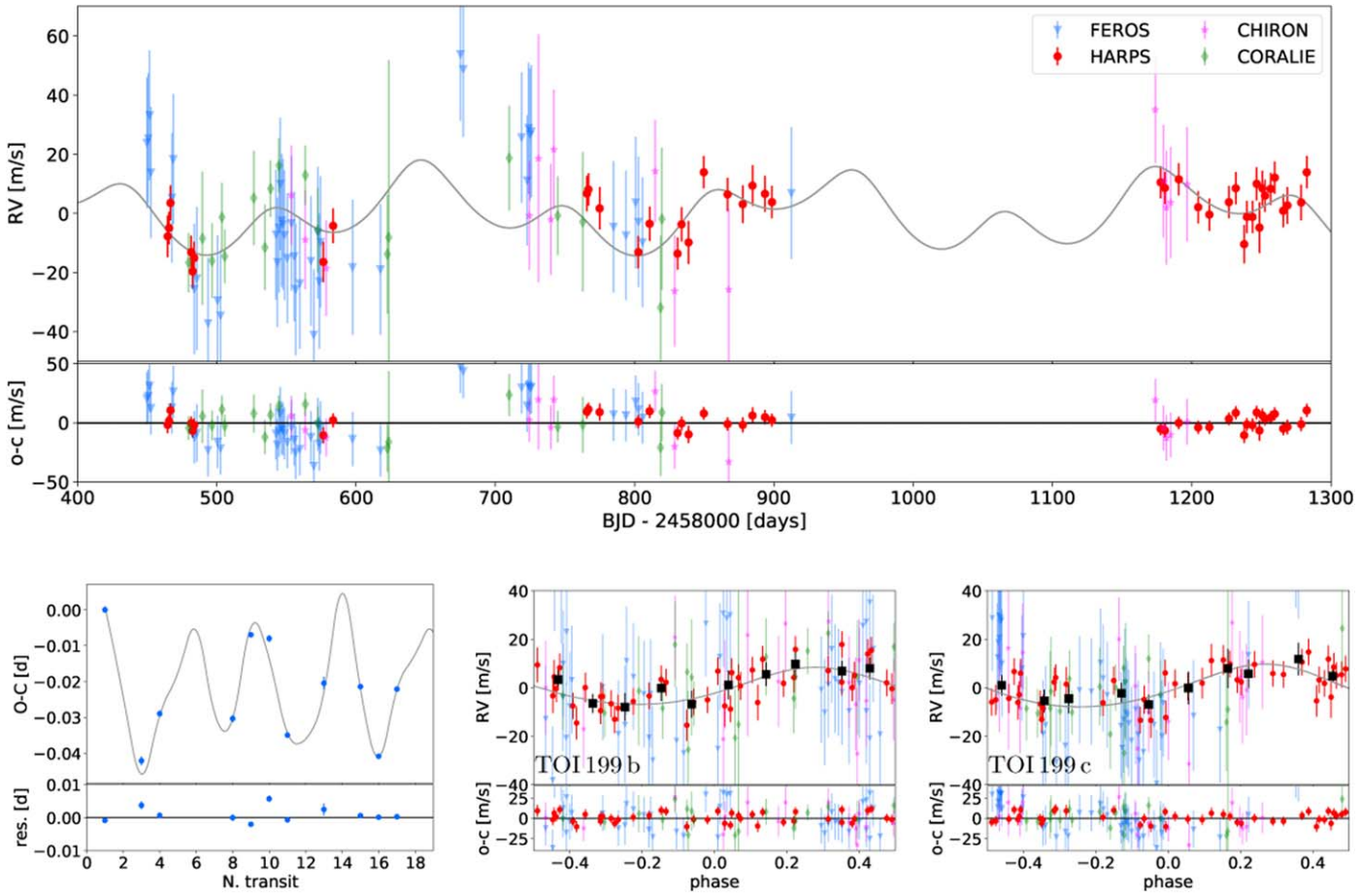

Figure 12. Top: RV measurements (FEROS: blue, HARPS: red, CHIRON: purple, and CORALIE: green) and best-fit two-planet model (gray line) for the combined data. Bottom left: TTVs (blue circles) and fitted model with `Exo-Striker` (gray line) for TOI-199 b (top panel) and residuals to the model (bottom panel). The model has been smoothed with a quadratic spline. Bottom center and right: phase-folded representation of the two planetary signals after the RV signal of the other companion was subtracted. The respective RV residuals are shown under each panel, accordingly. The more precise HARPS RVs, which are the main driver of the fit, are highlighted. The black squares show the binned phase-folded RVs.

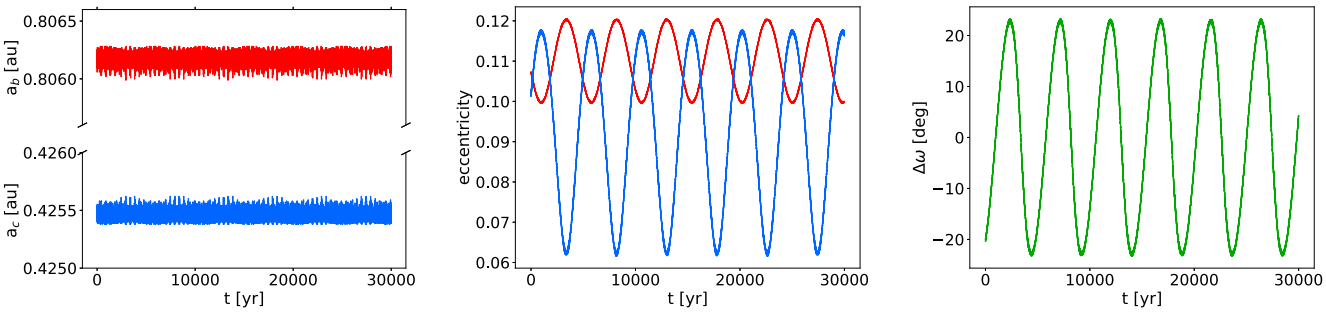

Figure 13. *N*-body orbital evolution of the TOI-199 system for an extent of 30,000 yr. The initial orbit is taken from our TTV+RV best fit (see Table 3) and is stable for at least 10 Myr. Left to right: evolution of the semimajor axes a_b (blue) and a_c (red), the eccentricities e_b (blue) and e_c (red), and the evolution of $\Delta\omega = \omega_b - \omega_c$, respectively. See the text for details.

evolve dynamically, are given for epoch BJD = 2,458,256.14.

3.4. Dynamical Stability

To examine the dynamical stability of the TOI-199 system, we first considered the classical Hill stability criterion (Gladman 1993) and the angular momentum deficiency criterion (AMD; Laskar & Petit 2017). In terms of Hill stability, we found that the two planets are separated by $\approx$7.7 R_H, well above the $\approx$2.4 R_H limit given by Gladman (1993; for initially circular orbits; however, the eccentricities of these planets are small). Likewise, the system is AMD stable, with values of $\beta = 0.3$ and $\beta_s = 0.02$, respectively (following Laskar & Petit 2017, Section 5), well below the $\beta = 1$ limit for collisions between the planets or the innermost planet and the star, respectively. Therefore, we do expect the TOI-199 Saturn-mass pair to be stable at the estimated orbits.

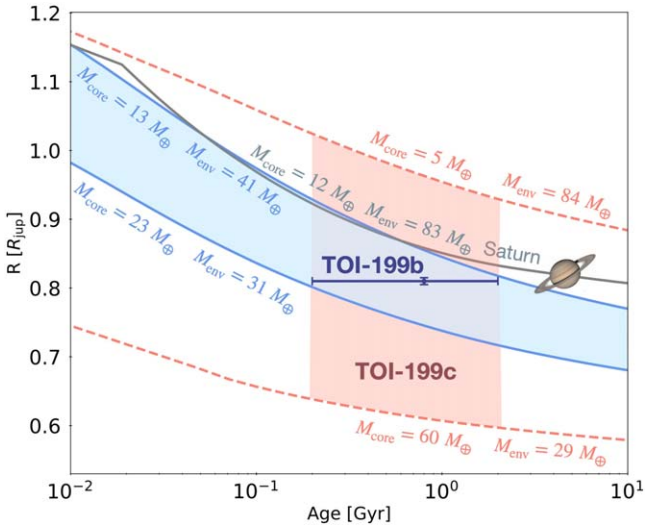

Figure 14. Evolution models of TOI-199 b and TOI-199 c compared to a simple model for Saturn. All models assume a central ice–rock core surrounded by a hydrogen and helium envelope of solar composition. M_{core} corresponds to the mass of the ice–rock core while M_{env} corresponds to the mass of the solar-composition envelope. The ranges of M_{core} and M_{env} compatible with the observational constraints are shown for TOI-199 b. The blue error bar corresponds to observational constraints on the age and the radius of TOI-199 b. We also show the range of radii expected for likely extreme compositions of TOI-199 c in red.

Nonetheless we aimed to analyze the dynamical evolution of the best fit, and study its properties. We performed a numerical *N*-body integration of the best-fit model with the Wisdom–Holman *N*-body algorithm (Wisdom & Holman 1991) for 10 Myr, adopting a small time step of $dt = 0.5$ days. Figure 13 shows the resulting evolution of the orbital semimajor axes, eccentricities, and $\Delta\omega$ for an extent of 30,000 yr. We find the system to be well separated with no significant changes in the semimajor axes during the 10 Myr *N*-body simulation. The eccentricities, however, osculate with notable amplitudes of $\approx$0.06 for e_b and $\approx$0.02 for e_c. We find that the planetary pair osculates in aligned geometry, with the secular apsidal angle $\Delta\omega = \omega_b - \omega_c$ librating around 0°, with a semiamplitude of $\sim$20°. The libration of the angle between the periapses $\Delta\omega$ is interesting, since it suggests that the planetary orbits must have been locked in secular apsidal alignment during the planet migration. Therefore, this libration of $\Delta\omega$ is an important remnant evidence of the planets' formation and orbital evolution during the disk phase.

4. Discussion

4.1. Possible Exomoons in the System

The possibility of stable exomoons orbiting the planets of the TOI-199 system is interesting for two reasons. On the one hand, exomoons could trigger TTVs variations in TOI-199 b, which might be misinterpreted as a TTV signal caused by a second planetary companion (Kipping & Yahalomi 2022). The relatively small Hill radius of TOI-199 b (R_{Hill} $\sim$0.014 au), and the orbital analysis of the RV and TTV data we performed in Section 3.3, strongly point to the existence of an outer Saturn-mass planet TOI-199 c, rather than an exomoon. Nonetheless, eliminating the exomoon hypothesis would strengthen the evidence for the existence of TOI-199 c even further. On the other hand, given the observational evidence of the existence of the Saturn-mass giant TOI-199 c, it is worth testing the possibility of exomoons around this companion. This planet orbits further out, so the Hill radius of dynamical influence is somewhat larger (R_{Hill} $\sim$0.03 au), positively affecting the potential exomoons' stability. Further, TOI-199 c resides in the habitable zone (HZ), which is intriguing for the existence of stable exomoon bodies. The gas giant was likely formed even further out beyond the ice line around TOI-199. Thus, initially icy exomoons, similar to those of Saturn, are possibly in the current warm orbit, and could become potentially habitable, ocean-like, or early Mars-like worlds (see Trifonov et al. 2020 for further discussion).

We study the possibility of stable exomoons in the system following the same numerical setup as in Trifonov et al. (2020), who tested the exomoon stability of the Saturn-mass pair of planets around the M-dwarf GJ 1148. The *N*-body test was done using the Wisdom–Holman algorithm (Wisdom & Holman 1991) modified to handle the evolution of test particles in the Jacobi coordinate system (Lee & Peale 2003), which allows for invertibility of the system's hierarchy (i.e., making either of the planets a central body in the system, enabling the testing of stable orbits around each planet). Our *N*-body simulations were performed with a very small time step of $dt = 0.01$ days and for a maximum of 1 Myr, which we find to be a good balance between CPU resources and the numerical accuracy of the run. We randomly seed an arbitrary number of 4000 "exomoon" mass-less test particles on circular prograde orbits around TOI-199 b & c. The semimajor axes of the test exomoons ranged randomly between the planetary Roche limit ($\sim$0.0003 au, for both planets), and the planetary Hill radius, where exomoons are expected to be stable. In addition, we studied the tidal interactions between the planets and the exomoons. We adopt Mars-like mass and radius for the exomoons ($m = 0.107\ M_\oplus$, $R = 0.53\ R_\oplus$). In contrast, for the massive planets TOI-199 b & c, we adopt masses and radii from our best-fit analysis (the radius of TOI-199 c is unknown as it does not transit; thus, we assumed the same radius as for TOI-199 b). We integrated their orbits with the EQTIDE[47] code (Barnes 2017), which calculates the tidal evolution of two bodies based on the models by Ferraz-Mello et al. (2008). For the rest of the numerical setup, we strictly follow the same EQTIDE prescription as in Trifonov et al. (2020).

The results from the test particle simulations are illustrated in Figure D1 for TOI-199 b, and Figure D2 for TOI-199 c, respectively. In the case of TOI-199 b, we found that only $\sim$48% of the test exomoons remained long-term stable with small eccentricities, usually those near the stability limit, which we found to be at $\sim$0.0055 au ($\sim$13 planet radii, $\sim$11.5 R_J). This stability limit is much smaller than the Hill radius of the planet. As was shown in Trifonov et al. (2020) the expected stability limit for prograde exomoons is $\sim$0.5 R_{Hill}, due to the dynamical perturbations of the second planet (see also Grishin et al. 2017). Similarly, for TOI-199 c the stability region was found to be $<$0.5 R_{Hill}, where $\sim$60% of the test particles survived for 1 Myr. As expected, the stable region around TOI-199 c is larger, close to 0.013 au ($\sim$27 R_J) from the planet. The tidal interactions, however, further limit the possible region where the exomoons could exist around both planets. The Saturn-mass planets likely have comparable rotational periods to Saturn ($\sim$10.5 hr), which will not be affected significantly

[47] https://github.com/RoryBarnes/EqTide

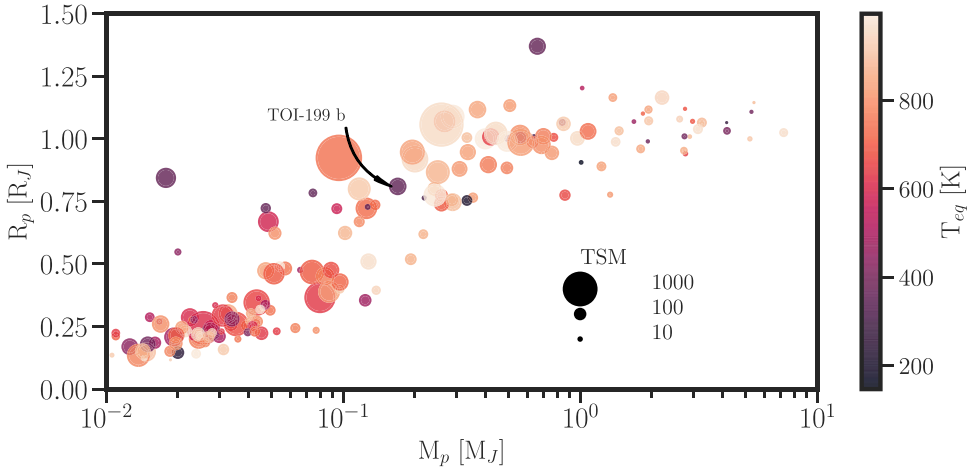

Figure 15. Mass–radius diagram for warm ($T_{eq} < 1000\ K$) giant planets with masses measured to better than 20% and radii measured to better than 10%, similar to our accuracies for TOI-199 b. The markers are color coded by equilibrium temperature and scaled by the TSM. TOI-199 b is significantly cooler than other well-characterized planets with similar masses and radii, and has a high TSM.

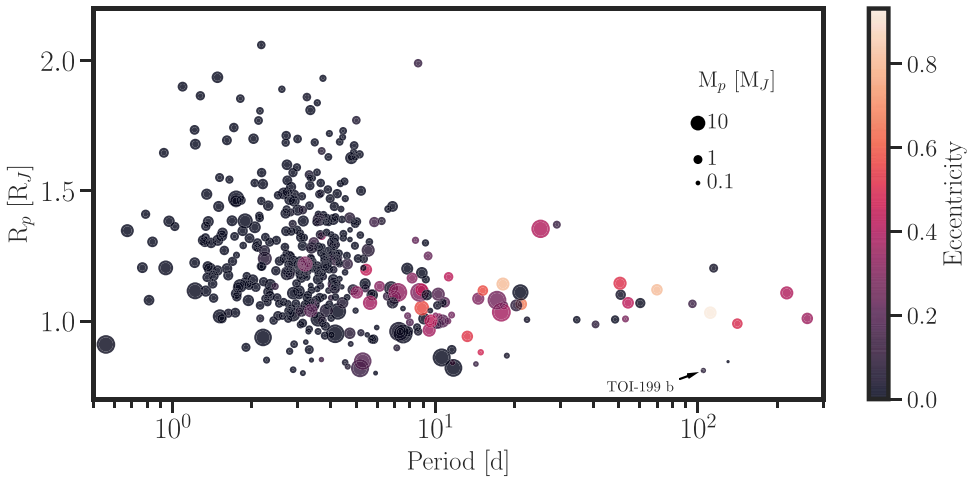

Figure 16. Radius–period diagram for giant planets with masses measured to better than 20% and radii measured to better than 10%, similar to our accuracies for TOI-199 b. The markers are color coded by eccentricity and scaled by planet mass. TOI-199 occupies a scarcely populated region of this space.

over the age of the system due to tidal interactions with the star. Therefore, closer Mars-like exomoons will drift away to longer orbits over time. Finally, we concluded that TOI-199 b is unlikely to host large exomoons because of the very limited range of semimajor axes of 0.0045–0.0055 au where such bodies can exist. For TOI-199 c habitable exomoons could exist in the range 0.0045–0.0125 au, comparable to the semimajor axes of the Galilean moons.

4.2. Interior Models

We modeled the interior evolution of both planets in the system using CEPAM (Guillot & Morel 1995) and a nongray atmosphere (Parmentier et al. 2015). We assumed simple structures consisting of a central dense core, composed of 50% ices and 50% rocks, surrounded by a hydrogen and helium envelope of solar composition. We use the P–ρ relationships from Hubbard & Marley (1989) to calculate the density in the core. The equation of state used for hydrogen and helium accounts for nonideal mixing effects (Howard & Guillot 2023; Chabrier et al. 2019).

Figure 14 shows the resulting evolution models and the observational constraints. Defining an approximate bulk metallicity as $Z \approx M_{\rm core}/M_{\rm tot}$ and assuming $Z_\odot = 0.015$, we find $Z/Z_\odot = 16$ to 28 for TOI-199 b. This is somewhat larger than what we obtain for a similarly simple model of Saturn although we stress that Saturn's enrichment corresponds to a narrower range of possibilities (between 12 and 15 according to Mankovich & Fuller 2021). However, most of the uncertainty comes from the poor constraint on the age of the system. An accurate determination of its age would thus greatly help to constrain the bulk metallicity of TOI-199 b (see also Müller & Helled 2023). We unfortunately do not have a measurement of the radius of TOI-199 c, as it does not transit. Using the same evolution models and a composition with cores between 5 and 60 $M_\oplus$ (bulk metallicity between 4 and 45), we obtain an expected radius of TOI-199 c between 0.6 and 1.03 R_J.

4.3. Atmospheric Characterization Potential

TOI-199 b is a very interesting target for atmospheric characterization through transmission spectroscopy. We computed the transmission spectroscopy metric (TSM; Kempton et al. 2018)

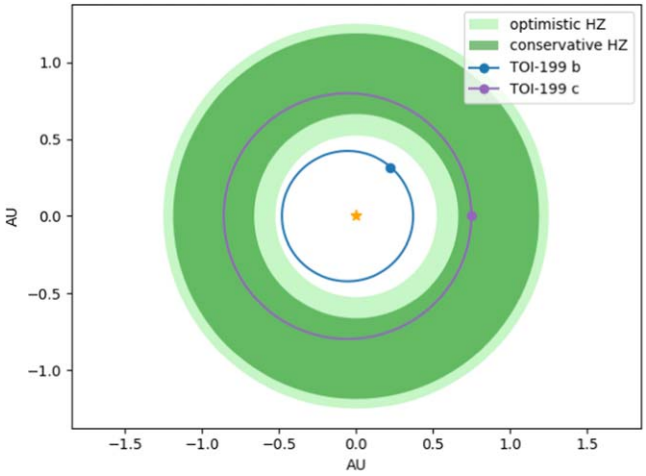

Figure 17. Orbital configuration of the TOI-199 system. The conservative and optimistic HZs are shown in dark and light green, respectively. TOI-199 c is in the HZ.

for TOI-199 b, finding a value of 107, above the TSM = 90 threshold recommended by Kempton et al. (2018). Compared to other well-characterized warm giants with similar masses and radii, it has a comparable TSM but is notably cooler (Figure 15), making it a unique target.

The intrinsic luminosities of both TOI-199 b and c are between a third to one times the present-day luminosity of Jupiter, implying that their atmospheric structure is mostly governed by the irradiation that they receive (see Parmentier et al. 2015). With a photospheric temperature expected to range between 250 and 350 K, TOI-199 b is an ideal candidate for the observation of the consequences of condensation of water in giant planet atmospheres (see Guillot et al. 2022).

4.4. The TOI-199 System in a Population Context

The TOI-199 system is composed of two giant planets. The inner planet, TOI-199 b, is a transiting warm giant with a $104.854^{+0.001}_{-0.002}$ day period, a 0.810 ± 0.005 R_J radius, and a 0.17 ± 0.02 M_J mass, comparable to those of Saturn ($R_S = 0.83$ R_J, $M_S = 0.30$ M_J). To place TOI-199 b in context within the exoplanet population, we plot the radius–period diagram (Figure 16) for giant planets ($R_p \geqslant 0.8$ R_J) with well-constrained masses and radii from the TEPCAT catalog (Southworth 2011).[48] TOI-199 b helps populate a so far very sparse region in the period–radius space. It is noticeably less massive, less dense, and less eccentric than its closest neighbors, and is the first warm exo-Saturn (i.e., a warm giant with mass and radius similar to those of Saturn) with mass measured to better than 20% and radius measured to better than 10%.

The outer planet, TOI-199 c, also falls within the warm giant parameter space at a period of $273.69^{+0.26}_{-0.22}$ days. With a minimum mass of $m \sin i = 0.28^{+0.02}_{-0.01}$ M_J, it is significantly more massive than the inner planet; as it does not transit, we cannot measure its radius. Given its orbital period, TOI-199 c falls into the conservative HZ, as defined by Kopparapu et al. (2014). The orbits of the two planets, and the conservative and optimistic HZ regions for TOI-199, are shown in Figure 17. However, given its minimum mass, TOI-199 c is presumably a gas giant, and as such does not possess a surface on which water could be found.

We use the stellar effective temperatures and luminosities listed in the NASA Exoplanet Archive[49] to compute the HZs defined by Kopparapu et al. (2014) for all stars with temperatures in the 2600–7200 K range and cataloged luminosities. While most exoplanet host stars (4092 out of the 5035 cataloged) fall in this temperature range, relatively few of those (897) have cataloged luminosities. In these, we find 159 planets in the conservative or optimistic HZs of their host stars, of which 138 have measured masses. Out of the planets with measured masses, the vast majority (111) have $M_p > 10$ $M_\oplus$, placing them in the Neptune-or-larger regime. True potentially habitable planets, with surfaces on which water could exist in a liquid state, are still rare. However, these giant planets, among which TOI-199 c falls, could still host potentially habitable exomoons.

5. Conclusions

We have presented the discovery and characterization of the TOI-199 system, composed of two warm giant planets. The inner planet, TOI-199 b, was first identified as a single transiter in TESS photometry, and confirmed using ASTEP, LCO, PEST, Hazelwood, and NEOSSat follow-up photometry, and HARPS, FEROS, CORALIE, and CHIRON RVs. The transits of TOI-199 b showed strong TTVs, pointing to the existence of a second planet in the system. From the joint analysis of the TTVs and RVs, we found that TOI-199 b has a $104.854^{+0.001}_{-0.002}$ day period, a mass of 0.17 ± 0.02 M_J, and a radius of 0.810 ± 0.005 R_J, making it the first precisely characterized warm exo-Saturn. Meanwhile, the outer non-transiting planet TOI-199 c has a period of $273.69^{+0.26}_{-0.22}$ days, placing it in the HZ, and a minimum mass of $0.28^{+0.02}_{-0.01}$ M_J.

We studied the dynamical stability and the potential for these planets to host exomoons. Our *N*-body simulations show that the system is stable, with no significant changes in the semimajor axes. The secular apsidal angle $\Delta\omega$, however, librates, suggesting the planets' orbits were locked in secular apsidal alignment during their migration. TOI-199 b is extremely unlikely to host large exomoons. TOI-199 c, on the other hand, could potentially host habitable exomoons, though as it does not transit these would be exceedingly difficult to detect.

TOI-199 b is a unique target for atmospheric characterization. It has a high TSM, and is cooler than other well-characterized giants with similar masses and radii, making it ideal for the study of water condensation in giant planet atmospheres.

TESS will observe one further transit of TOI-199 during Cycle 5, in Sector 67 (transit predicted for 2,460,143.85625384, 2023 July 18). We also predict transits on 2,460,248.7352902 (2023 October 31), 2,460,353.58791697 (2024 February 13), and 2,460,458.46233884 (2024 May 27), which will not be observed by TESS. Ground-based monitoring will thus be vital to the continued study of this TTV system.

[48] Available at https://www.astro.keele.ac.uk/jkt/tepcat/, accessed 2022 October 06.

[49] Retrieved 2022 June 02.

Acknowledgments

This paper includes data collected by the TESS mission, which are publicly available from the Mikulski Archive for Space Telescopes (MAST). Funding for the TESS mission is provided by NASA's Science Mission directorate. The specific observations analyzed can be accessed via DOI: 10.17909/cbph-wd44.

This research has made use of the Exoplanet Follow-up Observation Program website, which is operated by the California Institute of Technology, under contract with the National Aeronautics and Space Administration under the Exoplanet Exploration Program. We acknowledge the use of public TESS Alert data from the pipelines at the TESS Science Office and at the TESS Science Processing Operations Center.

Resources supporting this work were provided by the NASA High-End Computing (HEC) Program through the NASA Advanced Supercomputing (NAS) Division at Ames Research Center for the production of the SPOC data products.

Based on observations collected at the European Organisation for Astronomical Research in the Southern Hemisphere under ESO programs 0101.C-0510, 0102.C-0451, 0104.C-0413, 106.21ER.001, 0102.A-9003, 0102.A-9006, 0102.A-9011, 0102.A-9029, 0103.A-9008, and 0104.A-9007.

This research has made use of the Spanish Virtual Observatory (https://svo.cab.inta-csic.es) project funded by MCIN/AEI/10.13039/501100011033/ through grant PID2020-112949GB-I00.

T.T. acknowledges support by the DFG Research Unit FOR 2544 "Blue Planets around Red Stars" project No. KU 3625/2-1. T.T. further acknowledges support by the BNSF program "VIHREN-2021" project No. KP-06-DV/5.

A.J., R.B., and M.H. acknowledge support from ANID—Millennium Science Initiative—ICN12_009. A.J. acknowledges additional support from FONDECYT project 1210718. R.B. acknowledges support from FONDECYT Project 1120075 and from project IC120009 "Millennium Institute of Astrophysics (MAS)" of the Millenium Science Initiative. This work was funded by the Data Observatory Foundation.

The results reported herein benefited from collaborations and/or information exchange within the program "Alien Earths" (supported by the National Aeronautics and Space Administration under agreement No. 80NSSC21K0593) for NASA's Nexus for Exoplanet System Science (NExSS) research coordination network sponsored by NASA's Science Mission Directorate.

This work makes use of observations from the ASTEP telescope. ASTEP benefited from the support of the French and Italian polar agencies IPEV and PNRA in the framework of the Concordia station program, from OCA, INSU, Idex UCAJEDI (ANR- 15-IDEX-01) and ESA through the Science Faculty of the European Space Research and Technology Centre (ESTEC).

This work makes use of observations from the LCOGT network. Part of the LCOGT telescope time was granted by NOIRLab through the Mid-Scale Innovations Program (MSIP). MSIP is funded by NSF. K.A.C. acknowledges support from the TESS mission via subaward s3449 from MIT.

The postdoctoral fellowship of K.B. is funded by F.R.S.-FNRS grant T.0109.20 and by the Francqui Foundation.

The contributions of M.L., S.U., and S.S. have been carried out within the framework of the NCCR PlanetS supported by the Swiss National Science Foundation under grants 51NF40_182901 and 51NF40_205606. M.L. acknowledges support of the Swiss National Science Foundation under grant number PCEFP2_194576.

This research received funding from the European Research Council (ERC) under the European Union's Horizon 2020 research and innovation program (grant agreement n° 803193/BEBOP), and from the Science and Technology Facilities Council (STFC; grant n° ST/S00193X/1).

D.D. acknowledges support from the NASA Exoplanet Research Program grant 18-2XRP18_2-0136.

This work has made use of data from the European Space Agency (ESA) mission Gaia (https://www.cosmos.esa.int/gaia), processed by the Gaia Data Processing and Analysis Consortium (DPAC, https://www.cosmos.esa.int/web/gaia/dpac/consortium). Funding for the DPAC has been provided by national institutions, in particular the institutions participating in the Gaia Multilateral Agreement.

J.K. gratefully acknowledges the support of the Swedish National Space Agency (SNSA; DNR 2020-00104) and of the Swedish Research Council (VR: Etableringsbidrag 2017-04945).

M.T.P. acknowledges support of the ANID-Fondecyt Postdoctoral fellowship no. 3210253.

Facilities: TESS, ASTEP, LCOGT, PEST, NEOSSat, Hazelwood, Max Planck:2.2m (FEROS), ESO:3.6m (HARPS), Euler1.2m (CORALIE), CTIO:1.5m (CHIRON), and SOAR (HRCam).

Software: `tesseract` (F. Rojas et al. (2023, in preparation)), `CERES` (Brahm et al. 2017a), `juliet` (Espinoza et al. 2019), `ZASPE` (Brahm et al. 2017b), `radvel` (Fulton et al. 2018), `emcee` (Foreman-Mackey et al. 2013), `MultiNest` (Feroz et al. 2009), `PyMultiNest` (Buchner et al. 2014), `batman` (Kreidberg 2015), `celerite` (Foreman-Mackey et al. 2017), AstroImageJ (Collins et al. 2017), TAPIR (Jensen 2013), `Exo-Striker` (Trifonov 2019), EQTIDE (Barnes 2017), and limb-darkening (Espinoza & Jordán 2015).

Appendix A
RV and Activity Indices

In this appendix, we show the RVs and activity indicators (where applicable) obtained from the spectroscopic data. Tables A1 and A2 show the HARPS and FEROS results respectively, both obtained from the `ceres` pipeline. Table A3 shows the CORALIE results, obtained using the standard CORALIE DRS. Table A4 shows the CHIRON results, obtained following Jones et al. (2019).

Table A1
RV and Activity Indices Obtained from the HARPS Spectra

BJD—2,457,000 [day]	RV [km s^{-1}]	Bisector	FWHM	S/N	Hα	$log(R'_{HK})$	Na II	He I
1464.79399978	51.3356 ± 0.0052	−0.021 ± 0.007	7.7540	40	0.1205 ± 0.0016	−4.8668 ± 0.0356	0.1918 ± 0.0025	0.5018 ± 0.0037
1464.78179568	51.3470 ± 0.0046	−0.003 ± 0.006	7.7509	43	0.1237 ± 0.0014	−4.8177 ± 0.0296	0.1923 ± 0.0022	0.5066 ± 0.0034
1465.78521663	51.3439 ± 0.0022	−0.004 ± 0.003	7.7473	64	0.1254 ± 0.0010	−4.7620 ± 0.0187	0.1922 ± 0.0014	0.5031 ± 0.0023
1465.77425849	51.3450 ± 0.0021	0.002 ± 0.003	7.7630	66	0.1285 ± 0.0009	−4.7613 ± 0.0177	0.1907 ± 0.0013	0.5046 ± 0.0022
1466.77843100	51.3505 ± 0.0030	−0.008 ± 0.004	7.7446	55	0.1278 ± 0.0011	−4.7720 ± 0.0206	0.1921 ± 0.0016	0.4959 ± 0.0026
1466.76744544	51.3554 ± 0.0030	−0.003 ± 0.004	7.7638	55	0.1282 ± 0.0011	−4.7677 ± 0.0205	0.1908 ± 0.0016	0.4999 ± 0.0026
1481.68018901	51.3350 ± 0.0024	−0.001 ± 0.003	7.7732	62	0.1292 ± 0.0011	−4.6661 ± 0.0143	0.1979 ± 0.0016	0.5001 ± 0.0025
1481.69624159	51.3375 ± 0.0022	0.005 ± 0.003	7.7611	64	0.1294 ± 0.0011	−4.6882 ± 0.0149	0.1921 ± 0.0015	0.5017 ± 0.0024
1482.71116935	51.3298 ± 0.0027	0.009 ± 0.003	7.7900	59	0.1268 ± 0.0010	−4.7413 ± 0.0206	0.1938 ± 0.0015	0.5029 ± 0.0024
1483.75203132	51.3331 ± 0.0022	0.001 ± 0.003	7.7623	64	0.1276 ± 0.0010	−4.7612 ± 0.0188	0.1937 ± 0.0014	0.5058 ± 0.0023
1483.74069812	51.3355 ± 0.0021	0.004 ± 0.003	7.7595	66	0.1271 ± 0.0010	−4.7476 ± 0.0179	0.1940 ± 0.0014	0.5037 ± 0.0022
1576.52948882	51.3330 ± 0.0046	−0.014 ± 0.006	7.7801	43	0.1265 ± 0.0016	−5.4237 ± 0.1398	0.1907 ± 0.0022	0.4997 ± 0.0035
1583.54058377	51.3452 ± 0.0030	−0.002 ± 0.004	7.7792	55	0.1259 ± 0.0012	−5.0498 ± 0.0507	0.1980 ± 0.0017	0.4979 ± 0.0026
1765.74216151	51.3561 ± 0.0032	−0.003 ± 0.004	7.8046	54	0.1302 ± 0.0013	−4.7421 ± 0.0195	0.1988 ± 0.0018	0.5000 ± 0.0027
1766.80813997	51.3575 ± 0.0020	0.003 ± 0.002	7.7842	78	0.1294 ± 0.0009	−4.6460 ± 0.0131	0.2015 ± 0.0012	0.4983 ± 0.0020
1774.87929440	51.3546 ± 0.0049	0.003 ± 0.006	7.8038	42	0.1294 ± 0.0017	−4.7973 ± 0.0351	0.1970 ± 0.0024	0.4962 ± 0.0035
1774.88874566	51.3474 ± 0.0052	0.008 ± 0.007	7.8170	40	0.1321 ± 0.0018	−4.7826 ± 0.0346	0.1998 ± 0.0024	0.4983 ± 0.0036
1802.66127481	51.3363 ± 0.0020	0.002 ± 0.002	7.7880	95	0.1274 ± 0.0007	−4.6571 ± 0.0127	0.1954 ± 0.0010	0.5001 ± 0.0016
1810.75114647	51.3459 ± 0.0028	−0.005 ± 0.004	7.7686	57	0.1292 ± 0.0013	−4.7578 ± 0.0180	0.1945 ± 0.0016	0.4978 ± 0.0026
1830.82116768	51.3358 ± 0.0020	−0.004 ± 0.002	7.7822	85	0.1238 ± 0.0008	−4.7114 ± 0.0151	0.1925 ± 0.0010	0.5029 ± 0.0017
1833.70474847	51.3457 ± 0.0028	−0.006 ± 0.004	7.7964	57	0.1288 ± 0.0012	−4.6735 ± 0.0165	0.1925 ± 0.0016	0.5042 ± 0.0026
1838.71542850	51.3396 ± 0.0052	−0.012 ± 0.007	7.7865	40	0.1266 ± 0.0018	−4.7433 ± 0.0274	0.1962 ± 0.0025	0.5072 ± 0.0037
1849.67005564	51.3633 ± 0.0020	0.008 ± 0.002	7.7852	73	0.1263 ± 0.0010	−4.6783 ± 0.0142	0.1933 ± 0.0012	0.5039 ± 0.0020
1866.75015160	51.3558 ± 0.0025	−0.000 ± 0.003	7.8227	61	0.1223 ± 0.0010	−4.7484 ± 0.0206	0.1849 ± 0.0014	0.5093 ± 0.0023
1877.60993471	51.3525 ± 0.0038	0.002 ± 0.005	7.7812	48	0.1234 ± 0.0013	−4.7426 ± 0.0208	0.1882 ± 0.0017	0.5054 ± 0.0028
1884.59857785	51.3588 ± 0.0046	0.008 ± 0.006	7.8175	43	0.1279 ± 0.0016	−4.6631 ± 0.0191	0.1892 ± 0.0022	0.4970 ± 0.0033
1893.60218111	51.3560 ± 0.0034	−0.004 ± 0.004	7.7699	52	0.1254 ± 0.0012	−4.7414 ± 0.0190	0.1917 ± 0.0017	0.5006 ± 0.0027
1898.61246619	51.3532 ± 0.0020	0.001 ± 0.002	7.7709	73	0.1247 ± 0.0008	−4.7345 ± 0.0163	0.1911 ± 0.0011	0.5048 ± 0.0019
2177.64271415	51.3599 ± 0.0020	0.004 ± 0.003	7.7965	68	0.1365 ± 0.0011	−4.6513 ± 0.0145	0.1975 ± 0.0015	0.4980 ± 0.0024
2180.65538975	51.3580 ± 0.0020	0.002 ± 0.002	7.7665	80	0.1306 ± 0.0009	−4.7086 ± 0.0143	0.1975 ± 0.0012	0.5002 ± 0.0021
2190.65829783	51.3609 ± 0.0020	−0.001 ± 0.002	7.7770	73	0.1272 ± 0.0011	−4.7286 ± 0.0158	0.1927 ± 0.0014	0.5037 ± 0.0023
2204.58471260	51.3515 ± 0.0020	−0.002 ± 0.002	7.7795	83	0.1304 ± 0.0009	−4.6921 ± 0.0139	0.1990 ± 0.0012	0.5045 ± 0.0020
2212.60431636	51.3490 ± 0.0020	0.002 ± 0.002	7.7460	87	0.1243 ± 0.0008	−4.7019 ± 0.0138	0.1964 ± 0.0012	0.5074 ± 0.0019
2226.68671558	51.3532 ± 0.0020	0.007 ± 0.002	7.8213	69	0.1322 ± 0.0010	−4.7181 ± 0.0173	0.1964 ± 0.0014	0.4970 ± 0.0023
2231.56880343	51.3579 ± 0.0021	0.004 ± 0.003	7.7757	66	0.1279 ± 0.0011	−4.7062 ± 0.0161	0.1948 ± 0.0016	0.5016 ± 0.0025
2237.61010265	51.3390 ± 0.0040	−0.006 ± 0.005	7.7522	47	0.1220 ± 0.0015	−4.8071 ± 0.0257	0.1939 ± 0.0022	0.5079 ± 0.0034
2239.55155959	51.3482 ± 0.0020	−0.005 ± 0.002	7.7232	69	0.1220 ± 0.0010	−4.7566 ± 0.0166	0.1914 ± 0.0014	0.5086 ± 0.0023
2243.58440735	51.3482 ± 0.0020	−0.017 ± 0.002	7.7637	81	0.1262 ± 0.0009	−4.7494 ± 0.0154	0.1984 ± 0.0012	0.4996 ± 0.0020
2246.58730329	51.3594 ± 0.0024	−0.012 ± 0.003	7.7880	62	0.1284 ± 0.0012	−4.6911 ± 0.0170	0.1985 ± 0.0016	0.4994 ± 0.0026
2248.58606747	51.3446 ± 0.0069	0.005 ± 0.009	7.8496	33	0.1346 ± 0.0023	−5.1308 ± 0.0994	0.2088 ± 0.0034	0.5027 ± 0.0048
2250.61259800	51.3579 ± 0.0030	0.004 ± 0.004	7.8126	55	0.1316 ± 0.0013	−4.7977 ± 0.0232	0.1978 ± 0.0019	0.4986 ± 0.0029
2252.58098883	51.3554 ± 0.0020	0.003 ± 0.002	7.7913	78	0.1330 ± 0.0010	−4.6907 ± 0.0146	0.1983 ± 0.0013	0.5048 ± 0.0021
2256.58379243	51.3577 ± 0.0020	0.008 ± 0.002	7.7786	78	0.1249 ± 0.0009	−4.7789 ± 0.0167	0.1926 ± 0.0012	0.5055 ± 0.0020
2259.59184291	51.3615 ± 0.0020	−0.001 ± 0.002	7.7748	73	0.1245 ± 0.0010	−4.7708 ± 0.0174	0.1926 ± 0.0013	0.5065 ± 0.0022
2265.62666161	51.3503 ± 0.0024	−0.002 ± 0.003	7.7465	62	0.1239 ± 0.0011	−4.8104 ± 0.0231	0.1965 ± 0.0016	0.4979 ± 0.0025
2268.63412182	51.3521 ± 0.0036	−0.015 ± 0.005	7.8106	50	0.1287 ± 0.0014	−4.8145 ± 0.0280	0.1980 ± 0.0020	0.5015 ± 0.0031
2278.56738606	51.3531 ± 0.0032	−0.002 ± 0.004	7.7978	54	0.1265 ± 0.0013	−4.7587 ± 0.0234	0.1954 ± 0.0017	0.5059 ± 0.0027
2282.52973675	51.3633 ± 0.0020	0.001 ± 0.002	7.7765	78	0.1263 ± 0.0009	−4.8303 ± 0.0193	0.2002 ± 0.0011	0.5020 ± 0.0018

Table A2
RV and Activity Indices Obtained from the FEROS Spectra

BJD—2,457,000 [day]	RV [km s^{-1}]	Bisector	FWHM	S/N	Hα	$\log(R'_{HK})$	Na II	He I
1449.83201319	51.3599 ± 0.0069	−0.004 ± 0.011	10.0274	79	0.1291 ± 0.0022	−4.6161 ± 0.0289	0.1834 ± 0.0033	0.5030 ± 0.0057
1449.71864651	51.3394 ± 0.0054	−0.013 ± 0.009	9.9826	111	0.1313 ± 0.0015	−4.6156 ± 0.0210	0.1815 ± 0.0023	0.5026 ± 0.0039
1450.76285679	51.3461 ± 0.0055	−0.013 ± 0.009	10.0078	108	0.1299 ± 0.0016	−4.6040 ± 0.0212	0.1817 ± 0.0024	0.5006 ± 0.0041
1450.76988749	51.3538 ± 0.0057	−0.012 ± 0.009	10.0048	102	0.1323 ± 0.0017	−4.6358 ± 0.0235	0.1854 ± 0.0025	0.5021 ± 0.0042
1451.79336283	51.3548 ± 0.0057	−0.028 ± 0.009	10.0136	103	0.1295 ± 0.0017	−4.6330 ± 0.0239	0.1890 ± 0.0025	0.5023 ± 0.0044
1451.78645985	51.3606 ± 0.0057	−0.002 ± 0.009	9.9988	103	0.1298 ± 0.0017	−4.6299 ± 0.0236	0.1903 ± 0.0025	0.5039 ± 0.0043
1452.80242598	51.3384 ± 0.0067	−0.035 ± 0.011	10.0351	83	0.1251 ± 0.0020	−4.6715 ± 0.0313	0.1854 ± 0.0031	0.5002 ± 0.0054
1467.76807806	51.3298 ± 0.0056	−0.017 ± 0.009	10.0192	106	0.1345 ± 0.0016	−4.6849 ± 0.0249	0.1846 ± 0.0025	0.5017 ± 0.0041
1468.76772262	51.3428 ± 0.0060	−0.019 ± 0.010	10.0365	96	0.1360 ± 0.0018	−4.6456 ± 0.0251	0.1817 ± 0.0028	0.5055 ± 0.0046
1469.76959746	51.1795 ± 0.0058	−0.018 ± 0.009	10.0202	100	0.1291 ± 0.0018	−4.6321 ± 0.0234	0.1865 ± 0.0027	0.5037 ± 0.0045
1483.81130478	51.2990 ± 0.0061	−0.003 ± 0.010	10.1302	94	0.1345 ± 0.0017	−4.7680 ± 0.0660	0.1849 ± 0.0026	0.5054 ± 0.0045
1485.69646887	51.3025 ± 0.0119	−0.025 ± 0.017	10.0762	41	0.2045 ± 0.0058	−4.7093 ± 0.0825	0.1729 ± 0.0081	0.4653 ± 0.0117
1493.73812753	51.2874 ± 0.0067	−0.027 ± 0.011	10.0567	83	0.1448 ± 0.0022	−4.6505 ± 0.0326	0.1873 ± 0.0032	0.5004 ± 0.0056
1500.63798240	51.2951 ± 0.0062	−0.021 ± 0.010	10.0234	91	0.1430 ± 0.0020	−4.6571 ± 0.0269	0.1919 ± 0.0029	0.5043 ± 0.0051
1502.70459267	51.2900 ± 0.0069	−0.028 ± 0.011	10.0955	80	0.1559 ± 0.0024	−4.5820 ± 0.0281	0.1890 ± 0.0033	0.4965 ± 0.0054
1521.58004932	51.2470 ± 0.0056	−0.024 ± 0.009	10.0306	106	0.1433 ± 0.0017	−4.6306 ± 0.0233	0.1931 ± 0.0025	0.5044 ± 0.0041
1542.57046626	51.3174 ± 0.0060	−0.035 ± 0.010	10.1118	96	0.1319 ± 0.0018	−4.6890 ± 0.0292	0.1905 ± 0.0027	0.5047 ± 0.0045
1543.55517435	51.3081 ± 0.0056	−0.039 ± 0.009	10.1183	106	0.1340 ± 0.0017	−4.6422 ± 0.0244	0.1849 ± 0.0024	0.5099 ± 0.0041
1544.63920077	51.3197 ± 0.0058	−0.019 ± 0.009	10.1491	100	0.1426 ± 0.0019	−4.7059 ± 0.0375	0.1933 ± 0.0027	0.5075 ± 0.0047
1545.61458508	51.3345 ± 0.0072	−0.029 ± 0.011	10.1500	76	0.1321 ± 0.0024	−4.7325 ± 0.0479	0.1960 ± 0.0037	0.5021 ± 0.0062
1546.60962993	51.3222 ± 0.0073	−0.045 ± 0.011	10.2209	74	0.1492 ± 0.0025	−4.5902 ± 0.0365	0.1898 ± 0.0036	0.5011 ± 0.0060
1547.54838034	51.3209 ± 0.0063	−0.036 ± 0.010	10.1565	91	0.1409 ± 0.0020	−4.6714 ± 0.0286	0.1952 ± 0.0029	0.4914 ± 0.0048
1548.60710448	51.3172 ± 0.0059	−0.013 ± 0.010	10.1383	99	0.1421 ± 0.0018	−4.6428 ± 0.0300	0.1980 ± 0.0027	0.5019 ± 0.0047
1550.63138466	51.3094 ± 0.0058	−0.003 ± 0.009	10.1810	102	0.1408 ± 0.0018	−4.6807 ± 0.0367	0.1934 ± 0.0026	0.5031 ± 0.0046
1553.63083558	51.3212 ± 0.0086	−0.010 ± 0.013	10.2209	61	0.1461 ± 0.0031	−4.5733 ± 0.0522	0.1894 ± 0.0047	0.5110 ± 0.0077
1555.61367223	51.3100 ± 0.0058	−0.029 ± 0.009	10.1904	100	0.1331 ± 0.0018	−4.7084 ± 0.0363	0.1892 ± 0.0027	0.5092 ± 0.0047
1556.63579254	51.2989 ± 0.0071	−0.021 ± 0.011	10.2023	77	0.1389 ± 0.0024	−4.6131 ± 0.0425	0.1980 ± 0.0036	0.5017 ± 0.0060
1559.61969760	51.3009 ± 0.0064	−0.020 ± 0.010	10.1919	88	0.1434 ± 0.0022	−4.6768 ± 0.0421	0.1912 ± 0.0031	0.5054 ± 0.0053
1567.57829965	51.3085 ± 0.0056	−0.017 ± 0.009	10.1049	106	0.1301 ± 0.0018	−4.6912 ± 0.0307	0.1914 ± 0.0026	0.5057 ± 0.0045
1569.60503227	51.2835 ± 0.0064	−0.023 ± 0.010	10.1956	89	0.1329 ± 0.0020	−4.7453 ± 0.0601	0.1900 ± 0.0029	0.5023 ± 0.0051
1572.58523826	51.3181 ± 0.0069	−0.032 ± 0.011	10.2139	80	0.1330 ± 0.0023	−4.6869 ± 0.0467	0.1893 ± 0.0033	0.4985 ± 0.0057
1573.54735541	51.3016 ± 0.0084	−0.031 ± 0.013	10.1954	62	0.1544 ± 0.0031	−4.5939 ± 0.0391	0.1793 ± 0.0045	0.5042 ± 0.0075
1574.54805848	51.3149 ± 0.0068	−0.025 ± 0.011	10.1603	82	0.1415 ± 0.0022	−4.6917 ± 0.0391	0.1847 ± 0.0031	0.4994 ± 0.0055
1597.47834342	51.3063 ± 0.0086	−0.013 ± 0.013	10.1328	61	0.1431 ± 0.0030	−4.6326 ± 0.0483	0.1712 ± 0.0046	0.5005 ± 0.0074
1617.47697353	51.3056 ± 0.0062	−0.022 ± 0.010	10.1409	93	0.1354 ± 0.0019	−4.5700 ± 0.0482	0.1773 ± 0.0028	0.5070 ± 0.0048
1674.93453293	51.3783 ± 0.0075	−0.025 ± 0.011	10.0186	71	0.1312 ± 0.0024	−4.7272 ± 0.0608	0.1862 ± 0.0038	0.5134 ± 0.0060
1676.93586168	51.3733 ± 0.0087	−0.048 ± 0.013	9.9677	59	0.1390 ± 0.0032	−4.6440 ± 0.0566	0.1904 ± 0.0051	0.5115 ± 0.0076
1718.84166145	51.3502 ± 0.0062	−0.018 ± 0.010	10.0267	91	0.1362 ± 0.0020	−4.6830 ± 0.0346	0.2024 ± 0.0030	0.5057 ± 0.0051
1722.85657508	51.3357 ± 0.0061	−0.029 ± 0.010	10.0151	94	0.1450 ± 0.0021	−4.6067 ± 0.0246	0.1899 ± 0.0030	0.4967 ± 0.0048
1723.87675972	51.3533 ± 0.0066	−0.035 ± 0.010	10.0086	85	0.1394 ± 0.0022	−4.6187 ± 0.0290	0.2095 ± 0.0034	0.5060 ± 0.0054
1724.89283013	51.3512 ± 0.0072	−0.023 ± 0.011	10.0126	76	0.1385 ± 0.0024	−4.5978 ± 0.0298	0.1991 ± 0.0037	0.4994 ± 0.0061
1725.85732443	51.3523 ± 0.0070	−0.026 ± 0.011	10.0140	77	0.1332 ± 0.0023	−4.5306 ± 0.0281	0.1999 ± 0.0035	0.5056 ± 0.0058
1784.84308988	51.3200 ± 0.0066	−0.014 ± 0.011	9.9842	83	0.1262 ± 0.0021	−4.6930 ± 0.0291	0.1838 ± 0.0032	0.5004 ± 0.0053
1793.78206387	51.3171 ± 0.0057	−0.017 ± 0.009	10.0122	103	0.1311 ± 0.0017	−4.6046 ± 0.0219	0.1887 ± 0.0025	0.5059 ± 0.0043
1800.70371165	51.3282 ± 0.0069	0.002 ± 0.011	10.0512	80	0.1361 ± 0.0023	−4.6515 ± 0.0289	0.1813 ± 0.0034	0.5125 ± 0.0058
1802.71106430	51.3217 ± 0.0063	−0.013 ± 0.010	9.9732	89	0.1281 ± 0.0018	−4.7028 ± 0.0376	0.1800 ± 0.0028	0.5017 ± 0.0048
1805.73619653	51.3148 ± 0.0057	−0.005 ± 0.009	10.0003	102	0.1349 ± 0.0017	−4.6241 ± 0.0249	0.1847 ± 0.0025	0.5060 ± 0.0044
1912.53943145	51.3314 ± 0.0070	−0.015 ± 0.011	10.2001	79	0.1375 ± 0.0023	−4.6775 ± 0.0315	0.1976 ± 0.0035	0.5020 ± 0.0059

Table A3
RV and Activity Indices Obtained from the CORALIE Spectra

BJD—2,457,000 [day]	RV [km s^{-1}]	FWHM	Bisector	Hα
1479.75545134023	51,310.503 ± 0.009	9088.42 ± 12.85	–40.45 ± 12.72	0.2397 ± 0.0038
1489.74439708004	51,318.693 ± 0.022	9006.89 ± 12.74	13.24 ± 31.27	0.2398 ± 0.0068
1496.593841759954	51,311.109 ± 0.012	9055.17 ± 12.81	–44.33 ± 16.77	0.2341 ± 0.0045
1503.72372861998	51,325.855 ± 0.011	9110.66 ± 12.88	–72.14 ± 15.29	0.2358 ± 0.0041
1505.67841371009	51,312.657 ± 0.008	9104.72 ± 12.88	–22.37 ± 11.33	0.2356 ± 0.0035
1526.5760778198	51,332.347 ± 0.015	9173.53 ± 12.97	–47.52 ± 21.63	0.2270 ± 0.0050
1534.58861656999	51,315.643 ± 0.014	9091.04 ± 12.86	–94.11 ± 19.42	0.2294 ± 0.0049
1538.639787740074	51,335.519 ± 0.009	9098.83 ± 12.87	–49.80 ± 12.03	0.2261 ± 0.0035
1544.60949906986	51,343.382 ± 0.008	9082.49 ± 12.84	–66.87 ± 11.31	0.2337 ± 0.0034
1563.598259389866	51,340.052 ± 0.009	9098.37 ± 12.87	–55.33 ± 12.79	0.2343 ± 0.0037
1572.54610658996	51,321.501 ± 0.014	9144.88 ± 12.93	–69.62 ± 19.26	0.2394 ± 0.0049
1622.46025983011	51,313.385 ± 0.020	9159.30 ± 12.95	–37.24 ± 27.81	0.2236 ± 0.0058
1623.46099031018	51,319.046 ± 0.060	9304.44 ± 13.16	–149.08 ± 84.31	0.2113 ± 0.0134
1709.894646670204	51,345.850 ± 0.017	9101.04 ± 12.87	–103.87 ± 24.21	0.2419 ± 0.0059
1744.779055220075	51,326.377 ± 0.013	9150.97 ± 12.94	–61.98 ± 17.69	0.2552 ± 0.0047
1762.736076259986	51,324.292 ± 0.023	9144.08 ± 12.93	–116.84 ± 32.75	0.2499 ± 0.0070
1818.58744085999	51,295.316 ± 0.024	9150.28 ± 12.94	–44.14 ± 33.62	0.2352 ± 0.0068
1819.59875601018	51,325.253 ± 0.024	9186.31 ± 12.99	–42.85 ± 33.45	0.2201 ± 0.0067

Table A4
RV and Activity Indices Obtained from the CHIRON Spectra

BJD—2,457,000 [day]	RV [m s^{-1}]	Bisector	FWHM
1553.54058	6.0 ± 7.6	14.1 ± 27.4	12.090 ± 0.304
1563.54900	−9.1 ± 7.5	72.0 ± 29.0	12.088 ± 0.302
1578.55488	−18.7 ± 6.0	4.0 ± 36.5	12.033 ± 0.293
1723.90308	−1.8 ± 10.6	32.5 ± 23.4	12.254 ± 0.309
1724.89900	0.0 ± 10.8	−14.1 ± 22.8	12.219 ± 0.305
1730.93316	18.4 ± 39.1	−135.7 ± 98.1	12.188 ± 0.285
1739.87310	−2.2 ± 11.3	−76.0 ± 39.2	12.248 ± 0.306
1741.91746	21.4 ± 13.6	2.7 ± 42.8	12.205 ± 0.297
1814.73821	14.1 ± 8.6	−39.6 ± 31.2	12.135 ± 0.302
1828.71190	−26.4 ± 11.3	−12.0 ± 35.0	12.025 ± 0.309
1867.57241	−25.9 ± 22.7	−74.5 ± 55.4	12.116 ± 0.290
2173.80175	18.7 ± 7.3	−12.5 ± 35.1	12.134 ± 0.302
2173.80890	41.6 ± 11.7	5.0 ± 25.2	12.115 ± 0.307
2173.81606	53.4 ± 11.3	128.5 ± 43.5	12.163 ± 0.308
2179.73480	−3.1 ± 12.3	26.9 ± 35.4	12.139 ± 0.309
2179.74196	29.2 ± 11.1	40.8 ± 32.7	12.105 ± 0.314
2179.74911	4.0 ± 11.8	5.9 ± 39.6	12.081 ± 0.300
2181.72309	−11.2 ± 12.5	−19.6 ± 38.7	12.164 ± 0.312
2181.73025	−4.5 ± 11.3	3.8 ± 43.9	12.130 ± 0.311
2181.73740	21.5 ± 12.4	8.0 ± 42.3	12.137 ± 0.307
2184.73563	−6.7 ± 12.1	−99.8 ± 40.0	12.108 ± 0.298
2184.74278	20.4 ± 10.0	3.7 ± 39.9	12.094 ± 0.302
2184.74992	−6.9 ± 12.3	−90.0 ± 42.2	12.172 ± 0.300
2196.68466	34.3 ± 11.2	−9.6 ± 50.2	12.096 ± 0.315
2196.69181	−6.3 ± 12.8	−9.9 ± 36.7	12.116 ± 0.305
2196.69895	−2.6 ± 12.7	−41.2 ± 32.7	12.101 ± 0.307

Appendix B
Instrumental Priors and Posteriors for the TTV Extraction

In Table B1, we list the instrumental and GP prior and posterior distributions for the TTV extraction with `juliet`.

Table B1
Prior and Posterior Instrumental Parameter Distributions for the TTV Extraction with Juliet

Parameter	Prior[a]	Posterior
$q_{1,\mathrm{TESS}}$	$\mathcal{TN}(0.39, 0.1, 0, 1)$	0.30 ± 0.03
$q_{2,\mathrm{TESS}}$	$\mathcal{TN}(0.31, 0.1, 0, 1)$	$0.36^{+0.05}_{-0.06}$
$q_{1,\mathrm{ASTEP}}$	$\mathcal{TN}(0.5, 0.1, 0, 1)$	0.62 ± 0.06
$q_{2,\mathrm{ASTEP}}$	$\mathcal{TN}(0.35, 0.1, 0, 1)$	0.07 ± 0.04
$q_{1,\mathrm{PEST}}$	$\mathcal{TN}(0.5, 0.1, 0, 1)$	0.83 ± 0.07
$q_{2,\mathrm{PEST}}$	$\mathcal{TN}(0.5, 0.1, 0, 1)$	$0.49^{+0.06}_{-0.07}$
$q_{1,\mathrm{NEOSsat}}$	$\mathcal{TN}(0.59, 0.1, 0, 1)$	$0.67^{+0.06}_{-0.07}$
$q_{2,\mathrm{NEOSSat}}$	$\mathcal{TN}(0.39, 0.1, 0, 1)$	0.41 ± 0.07
$q_{1,\mathrm{Hwd}}$	$\mathcal{TN}(0.5, 0.1, 0, 1)$	$0.50^{+0.08}_{-0.07}$
$q_{2,\mathrm{Hwd}}$	$\mathcal{TN}(0.35, 0.1, 0, 1)$	$0.35^{+0.08}_{-0.07}$
$q_{1,\mathrm{LCO},1}$	$\mathcal{TN}(0.33, 0.1, 0, 1)$	$0.32^{+0.08}_{-0.07}$
$q_{2,\mathrm{LCO},1}$	$\mathcal{TN}(0.29, 0.1, 0, 1)$	0.30 ± 0.07
$q_{1,\mathrm{LCO},2}$	$\mathcal{TN}(0.68, 0.1, 0, 1)$	$0.61^{+0.08}_{-0.06}$
$q_{2,\mathrm{LCO},2}$	$\mathcal{TN}(0.45, 0.1, 0, 1)$	$0.43^{+0.07}_{-0.06}$
$q_{1,\mathrm{LCO},3}$	$\mathcal{TN}(0.41, 0.1, 0, 1)$	$0.29^{+0.07}_{-0.06}$
$q_{2,\mathrm{LCO},3}$	$\mathcal{TN}(0.32, 0.1, 0, 1)$	$0.22^{+0.07}_{-0.06}$
$q_{1,\mathrm{LCO},4}$	$\mathcal{TN}(0.41, 0.1, 0, 1)$	$0.33^{+0.07}_{-0.06}$
$q_{2,\mathrm{LCO},4}$	$\mathcal{TN}(0.32, 0.1, 0, 1)$	$0.25^{+0.07}_{-0.06}$
$q_{1,\mathrm{LCO},5}$	$\mathcal{TN}(0.68, 0.1, 0, 1)$	0.71 ± 0.07
$q_{2,\mathrm{LCO},5}$	$\mathcal{TN}(0.45, 0.1, 0, 1)$	0.43 ± 0.07
$q_{1,\mathrm{LCO},6}$	$\mathcal{TN}(0.41, 0.1, 0, 1)$	$0.29^{+0.07}_{-0.08}$
$q_{2,\mathrm{LCO},6}$	$\mathcal{TN}(0.32, 0.1, 0, 1)$	$0.25^{+0.06}_{-0.05}$
$m_{\mathrm{d,TESS},2}$	1.0 (fixed)	1.0 (fixed)
$m_{\mathrm{flux,TESS},2}$	$\mathcal{N}(0, 0.1)$	$0.0002^{+0.0012}_{-0.0013}$
$\sigma_{\mathrm{TESS},2}$	$\mathcal{J}(0.1, 1000)$	402 ± 8
$m_{\mathrm{d,TESS},10}$	1.0 (fixed)	1.0 (fixed)
$m_{\mathrm{flux,TESS},10}$	$\mathcal{N}(0, 0.1)$	0.003 ± 0.002
$\sigma_{\mathrm{TESS},10}$	$\mathcal{J}(0.1, 1000)$	327 ± 13
$m_{\mathrm{d,TESS},13}$	1.0 (fixed)	1.0 (fixed)
$m_{\mathrm{flux,TESS},13}$	$\mathcal{N}(0, 0.1)$	$-0.0007^{+0.0006}_{-0.0005}$
$\sigma_{\mathrm{TESS},13}$	$\mathcal{J}(0.1, 1000)$	371^{+10}_{-11}
$m_{\mathrm{d,TESS},29}$	1.0 (fixed)	1.0 (fixed)
$m_{\mathrm{flux,TESS},29}$	$\mathcal{N}(0, 0.1)$	$0.0010^{+0.0006}_{-0.0005}$
$\sigma_{\mathrm{TESS},29}$	$\mathcal{J}(0.1, 1000)$	641 ± 9
$m_{\mathrm{d,TESS},32}$	1.0 (fixed)	1.0 (fixed)
$m_{\mathrm{flux,TESS},32}$	$\mathcal{N}(0, 0.1)$	$0.006^{+0.005}_{-0.006}$
$\sigma_{\mathrm{TESS},32}$	$\mathcal{J}(0.1, 1000)$	419^{+8}_{-7}
$m_{\mathrm{d,TESS},36}$	1.0 (fixed)	1.0 (fixed)
$m_{\mathrm{flux,TESS},36}$	$\mathcal{N}(0, 0.1)$	0.0012 ± 0.0008
$\sigma_{\mathrm{TESS},36}$	$\mathcal{J}(0.1, 1000)$	604^{+10}_{-9}
$m_{\mathrm{flux,TESS},63}$	$\mathcal{N}(0, 0.1)$	$-0.0003^{+0.0030}_{-0.0028}$
$\sigma_{\mathrm{TESS},63}$	$\mathcal{J}(0.1, 1000)$	493 ± 8
$m_{\mathrm{d,ASTEP},1}$	1.0 (fixed)	1.0 (fixed)
$m_{\mathrm{flux,ASTEP},1}$	$\mathcal{N}(0, 0.1)$	0.0004 ± 0.0001
$\sigma_{\mathrm{ASTEP},1}$	$\mathcal{J}(0.1, 1000)$	960^{+34}_{-25}
$m_{\mathrm{d,ASTEP},2}$	1.0 (fixed)	1.0 (fixed)
$m_{\mathrm{flux,ASTEP},2}$	$\mathcal{N}(0, 0.1)$	0.00027 ± 0.00007
$\sigma_{\mathrm{ASTEP},2}$	$\mathcal{J}(0.1, 1000)$	$999.1^{+0.9}_{-0.6}$
$m_{\mathrm{d,ASTEP},3}$	1.0 (fixed)	1.0 (fixed)
$m_{\mathrm{flux,ASTEP},3}$	$\mathcal{N}(0, 0.1)$	-0.00088 ± 0.00007
$\sigma_{\mathrm{ASTEP},3}$	$\mathcal{J}(0.1, 1000)$	998^{+2}_{-1}
$m_{\mathrm{d,PEST}}$	1.0 (fixed)	1.0 (fixed)
$m_{\mathrm{flux,PEST}}$	$\mathcal{N}(0, 0.1)$	$0.00004^{+0.00008}_{-0.00009}$
σ_{PEST}	$\mathcal{J}(0.1, 1000)$	996 ± 3
$m_{\mathrm{d,NEOSSat}}$	1.0 (fixed)	1.0 (fixed)
$m_{\mathrm{flux,NEOSSat}}$	$\mathcal{N}(0, 0.1)$	-0.00002 ± 0.00003
$\sigma_{\mathrm{NEOSSat}}$	$\mathcal{J}(0.1, 1000)$	$999.92^{+0.08}_{-0.05}$
$m_{\mathrm{d,Hwd}}$	1.0 (fixed)	1.0 (fixed)
$m_{\mathrm{flux,Hwd}}$	$\mathcal{N}(0, 0.1)$	-0.050 ± 0.0001
σ_{Hwd}	$\mathcal{J}(0.1, 1000)$	995^{+5}_{-3}
$m_{\mathrm{d,LCO},1}$	1.0 (fixed)	1.0 (fixed)
$m_{\mathrm{flux,LCO},1}$	$\mathcal{N}(0, 0.1)$	$-0.000003^{+0.000075}_{-0.000071}$
$\sigma_{\mathrm{LCO},1}$	$\mathcal{J}(0.1, 1000)$	779^{+91}_{-95}
$m_{\mathrm{d,LCO},2}$	1.0 (fixed)	1.0 (fixed)
$m_{\mathrm{flux,LCO},2}$	$\mathcal{N}(0, 0.1)$	-0.0003 ± 0.0002
$\sigma_{\mathrm{LCO},2}$	$\mathcal{J}(0.1, 1000)$	989^{+9}_{-7}
$m_{\mathrm{d,LCO},3}$	1.0 (fixed)	1.0 (fixed)
$m_{\mathrm{flux,LCO},3}$	$\mathcal{N}(0, 0.1)$	0.0003 ± 0.0001
$\sigma_{\mathrm{LCO},3}$	$\mathcal{J}(0.1, 1000)$	994^{+7}_{-4}
$m_{\mathrm{d,LCO},4}$	1.0 (fixed)	1.0 (fixed)
$m_{\mathrm{flux,LCO},4}$	$\mathcal{N}(0, 0.1)$	-0.0001 ± 0.0001
$\sigma_{\mathrm{LCO},4}$	$\mathcal{J}(0.1, 1000)$	986^{+14}_{-9}
$m_{\mathrm{d,LCO},5}$	1.0 (fixed)	1.0 (fixed)
$m_{\mathrm{flux,LCO},5}$	$\mathcal{N}(0, 0.1)$	-0.00003 ± 0.00014
$\sigma_{\mathrm{LCO},5}$	$\mathcal{J}(0.1, 1000)$	990^{+12}_{-7}
$m_{\mathrm{d,LCO},6}$	1.0 (fixed)	1.0 (fixed)
$m_{\mathrm{flux,LCO},6}$	$\mathcal{N}(0, 0.1)$	-0.0082 ± 0.00006
$\sigma_{\mathrm{LCO},6}$	$\mathcal{J}(0.1, 1000)$	998^{+2}_{-1}
$\sigma_{\mathrm{GP,\ TESS,\ 2}}$	$\mathcal{J}(0.0023, 0.0052)$	$0.0031^{+0.0005}_{-0.0007}$
$\rho_{\mathrm{GP,\ TESS,\ 2}}$	$\mathcal{J}(3.0, 5.9)$	$4.0^{+0.5}_{-0.7}$
$\sigma_{\mathrm{GP,\ TESS,\ 10}}$	$\mathcal{J}(0.007, 0.010)$	$0.0086^{+0.0005}_{-0.0006}$
$\rho_{\mathrm{GP,\ TESS,\ 10}}$	$\mathcal{J}(0.63, 0.79)$	$0.70^{+0.03}_{-0.04}$
$\sigma_{\mathrm{GP,\ TESS,\ 13}}$	$\mathcal{J}(0.0028, 0.0036)$	0.0031 ± 0.0002
$\rho_{\mathrm{GP,\ TESS,\ 13}}$	$\mathcal{J}(0.64, 0.81)$	$0.71^{+0.03}_{-0.04}$
$\sigma_{\mathrm{GP,\ TESS,\ 29}}$	$\mathcal{J}(0.0032, 0.0040)$	0.0035 ± 0.0002
$\rho_{\mathrm{GP,\ TESS,\ 29}}$	$\mathcal{J}(0.39, 0.47)$	0.42 ± 0.02
$\sigma_{\mathrm{GP,\ TESS,\ 32}}$	$\mathcal{J}(0.0053, 0.0265)$	$0.009^{+0.002}_{-0.004}$
$\rho_{\mathrm{GP,\ TESS,\ 32}}$	$\mathcal{J}(6.1, 20.0)$	9^{+2}_{-3}
$\sigma_{\mathrm{GP,\ TESS,\ 36}}$	$\mathcal{J}(0.0049, 0.0061)$	0.0054 ± 0.0003
$\rho_{\mathrm{GP,\ TESS,\ 36}}$	$\mathcal{J}(0.39, 0.47)$	0.42 ± 0.02
$\sigma_{\mathrm{GP,\ TESS,\ 63}}$	$\mathcal{J}(0.0049, 0.0141)$	$0.007^{+0.001}_{-0.002}$
$\rho_{\mathrm{GP,\ TESS,\ 63}}$	$\mathcal{J}(3.2, 7.0)$	$4.2^{+0.6}_{-0.8}$

Notes:
[a] $\mathcal{U}(a, b)$ indicates a uniform distribution between a and b; $\mathcal{TN}(a, b)$ a normal distribution with mean a and standard deviation b $\mathcal{N}(a, b, c, d)$ a normal distribution with mean a, standard deviation b, limited to the $[c, d]$ range; $\mathcal{J}(a, b)$ a Jeffreys or log-uniform distribution between a and b.

Appendix C
Posterior Probability Distributions

In this appendix, we show the posterior probability distribution of the joint TTV+RV modeling with `Exo-Striker`. For ease of viewing, we have separated the corner plots into fitted planetary parameters (Figures C1 and C2), derived planetary parameters (Figure C3), and instrumental RV parameters (Figure C4).

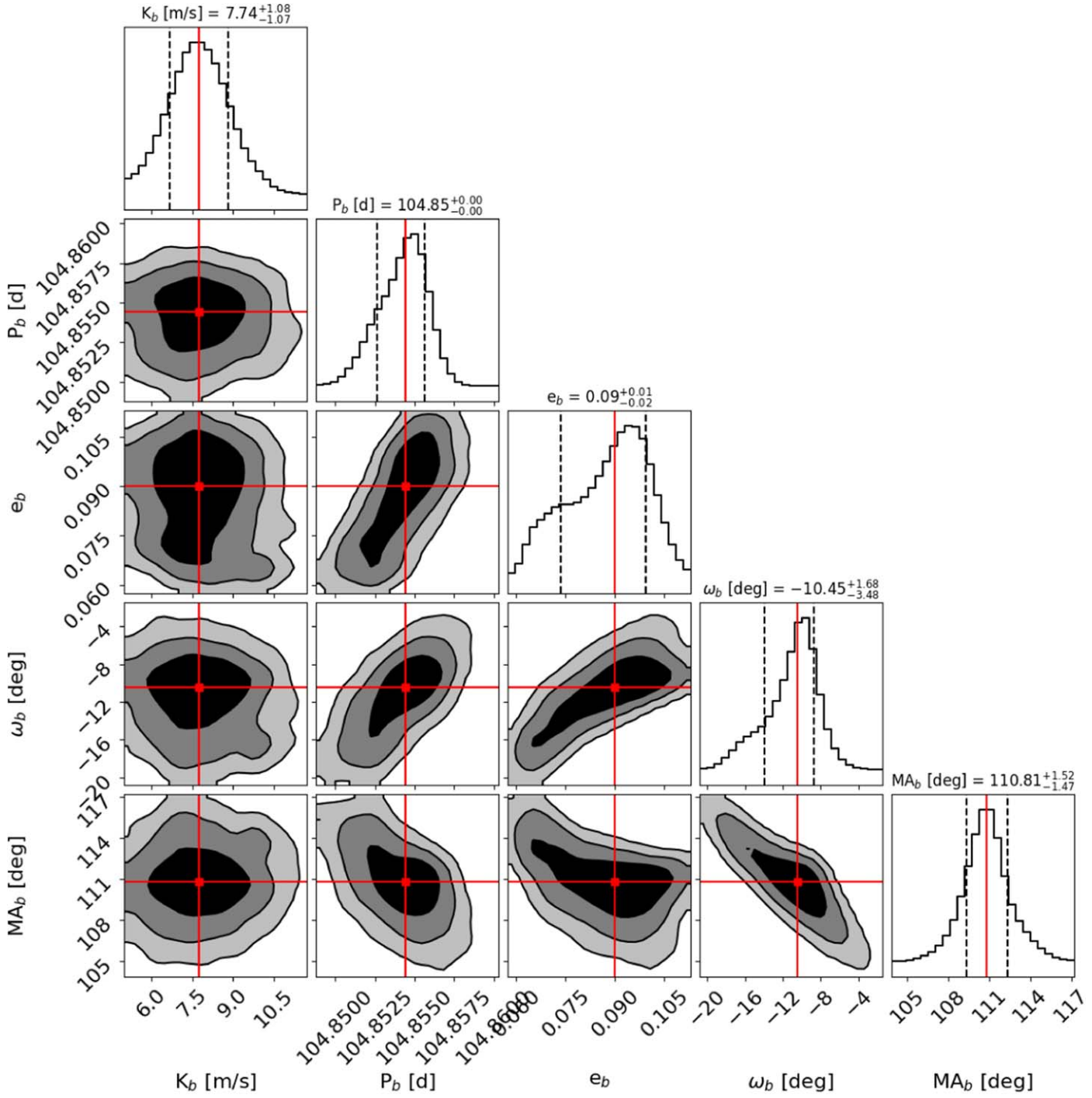

Figure C1. Corner plot of the posterior distributions of the fitted planet parameters for TOI-199 b for the joint modeling of the TESS and ASTEP TTVs, and the HARPS, FEROS, CHIRON, and CORALIE RVs. The distributions are explored using nested sampling. The red crosses indicate the median values, and the black contour lines the 1σ, 2σ, and 3σ confidence levels. For ω_b, note that it is a circular argument and thus, e.g., $-10^\circ = 350^\circ$.

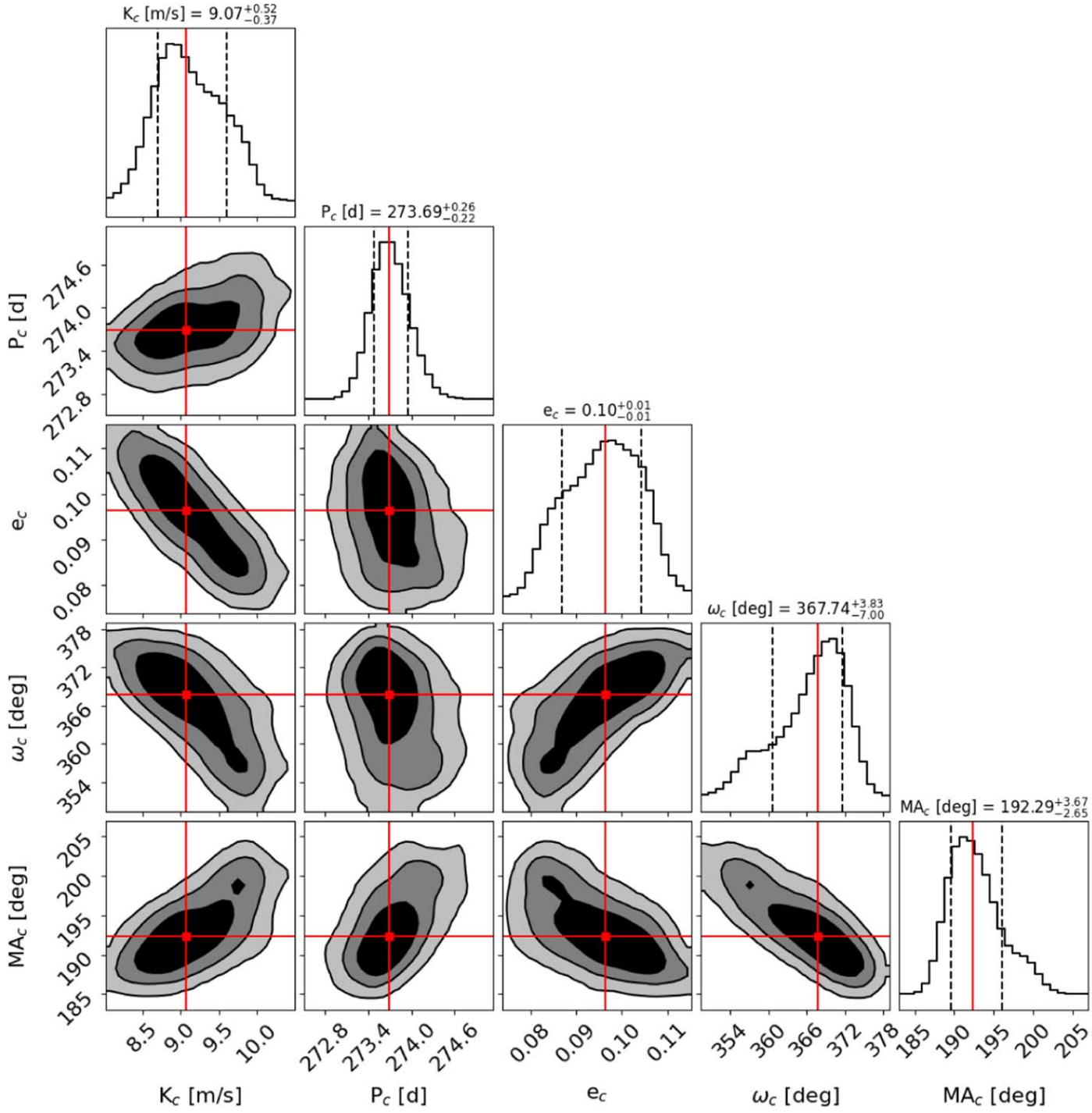

Figure C2. Corner plot of the posterior distributions of the planet parameters for TOI-199 c from the joint modeling of the TESS and ASTEP TTVs, and the HARPS, FEROS, CHIRON, and CORALIE RVs. The distributions are explored using nested sampling. The red crosses indicate the median values, and the black contour lines the 1σ, 2σ, and 3σ confidence levels. For ω_c, note that it is a circular argument and thus, e.g., $370^\circ = 10^\circ$.

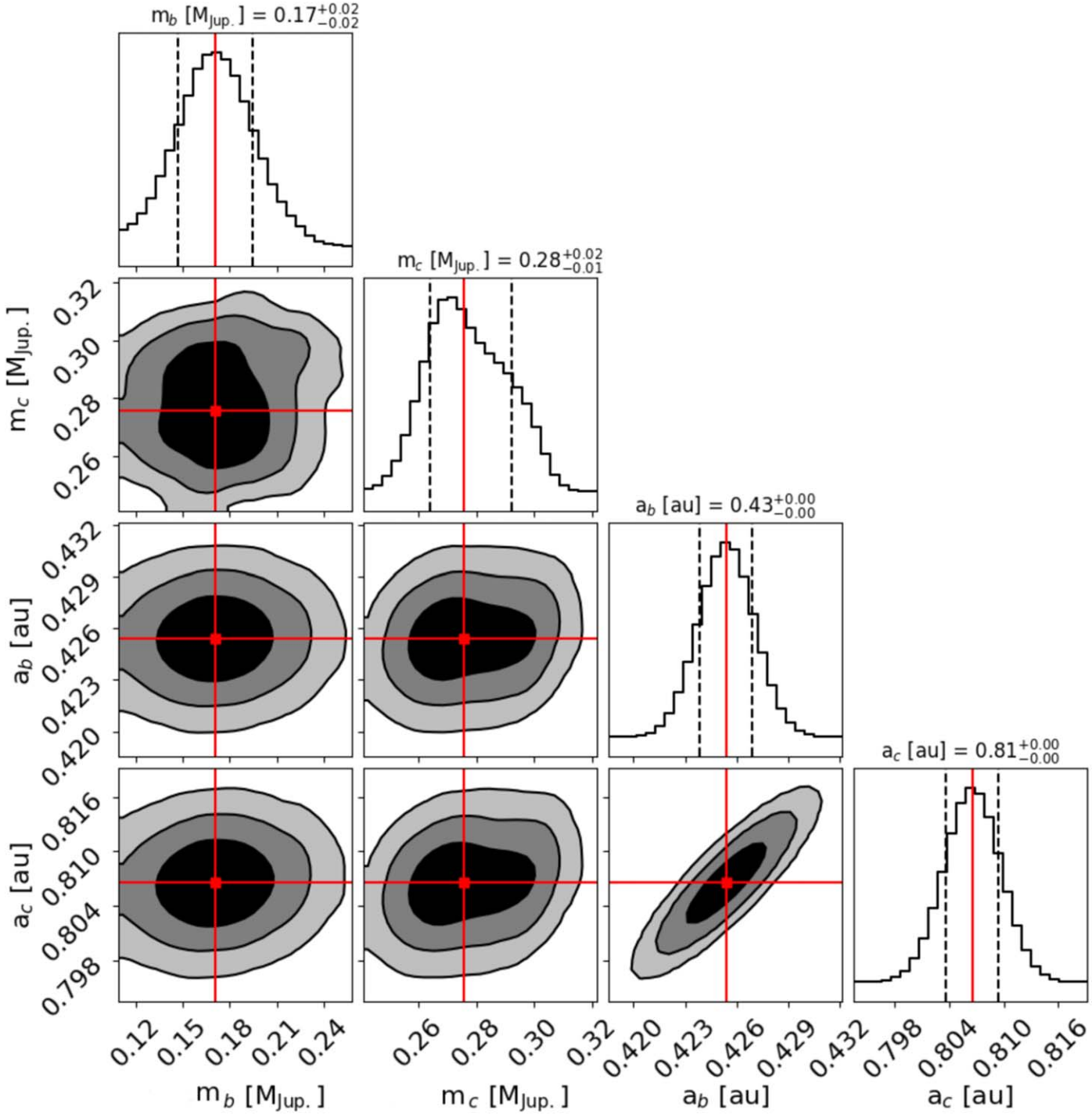

Figure C3. Corner plot of the posterior distributions of the derived planet parameters for the joint modeling of the TESS and ASTEP TTVs, and the HARPS, FEROS, CHIRON, and CORALIE RVs. The distributions are explored using nested sampling. The red crosses indicate the median values, and the black contour lines the 1σ, 2σ, and 3σ confidence levels.

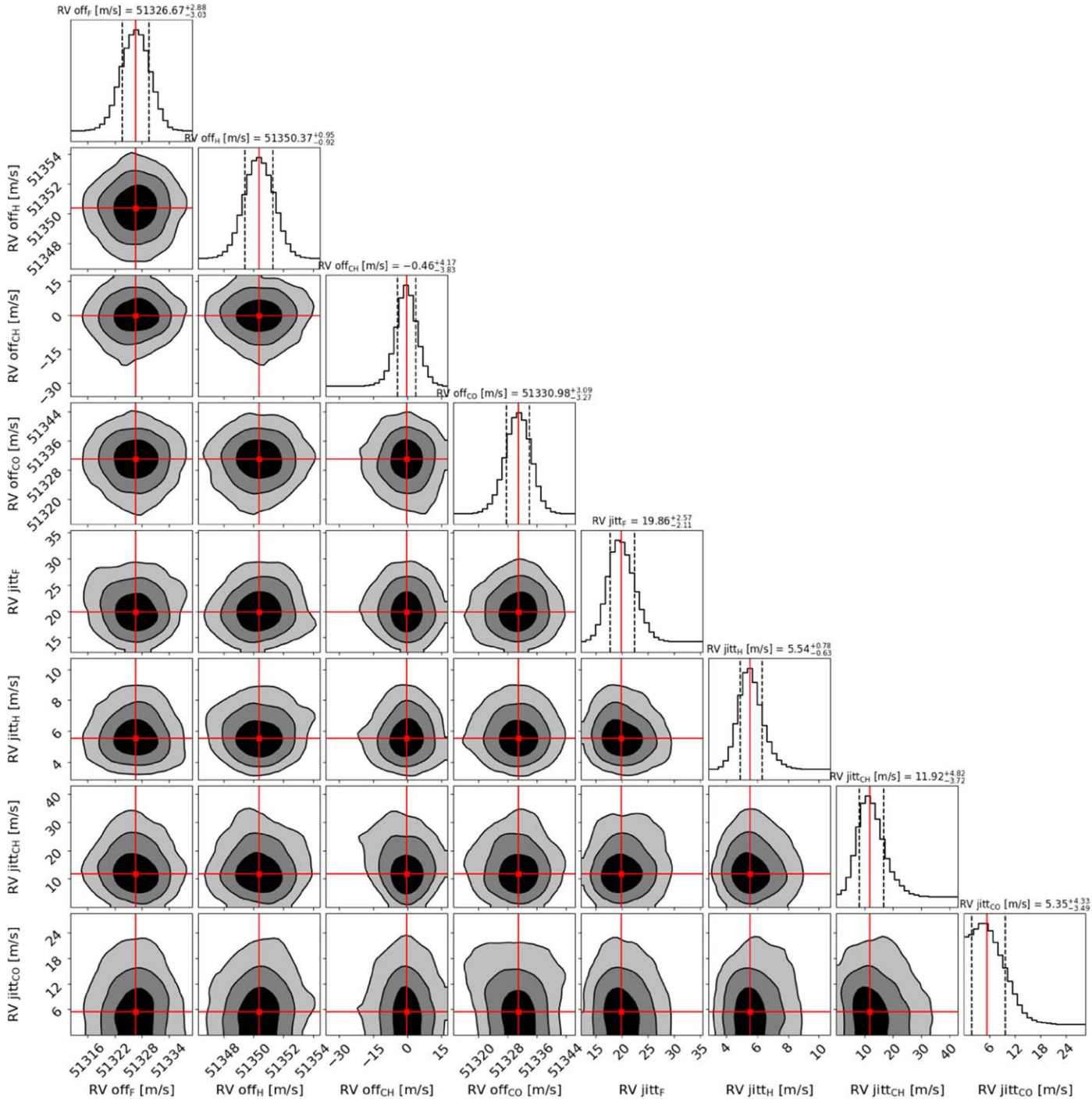

Figure C4. Corner plot of the posterior distributions of the instrumental RV parameters for the joint modeling of the TESS and ASTEP TTVs, and the HARPS, FEROS, CHIRON, and CORALIE RVs. The distributions are explored using nested sampling. The red crosses indicate the median values, and the black contour lines the 1σ, 2σ, and 3σ confidence levels. Subindex H refers to HARPS, F to FEROS, CH to CHIRON, and CO to CORALIE.

Appendix D
Exomoon Dynamical Evolution

In Figures D1 and D2, we show the dynamical evolution of the test particles used in the exomoon analysis described in Section 4.1.

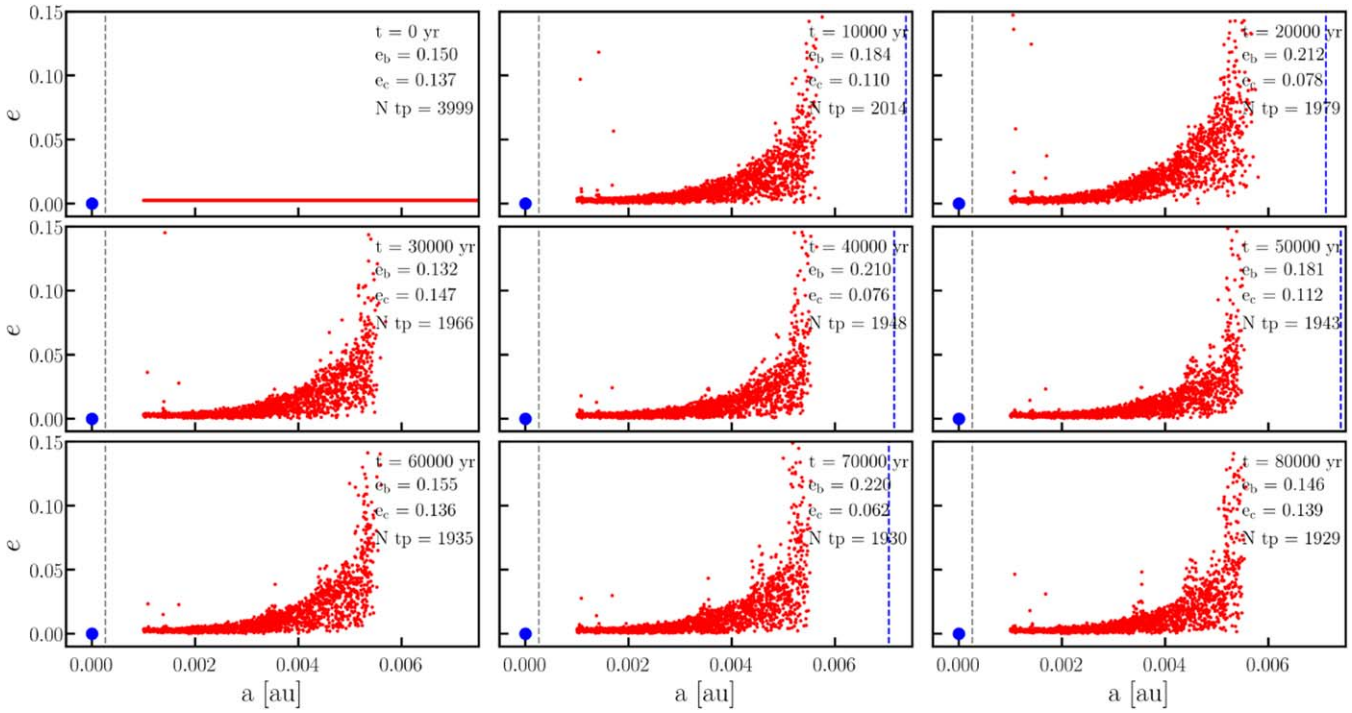

Figure D1. Evolution of mass-less test particles (i.e., exomoons) around TOI-199 b, under gravitational perturbation of the outer planet. Shown are the position of TOI-199 b (blue dot), the planetary Roche limit (gray dashed line), and the planetary 0.5 $R_{\rm Hill}$ (blue dashed line), which scales with $(1 - e_b)$ due to the dynamical perturbations of TOI-199 c.

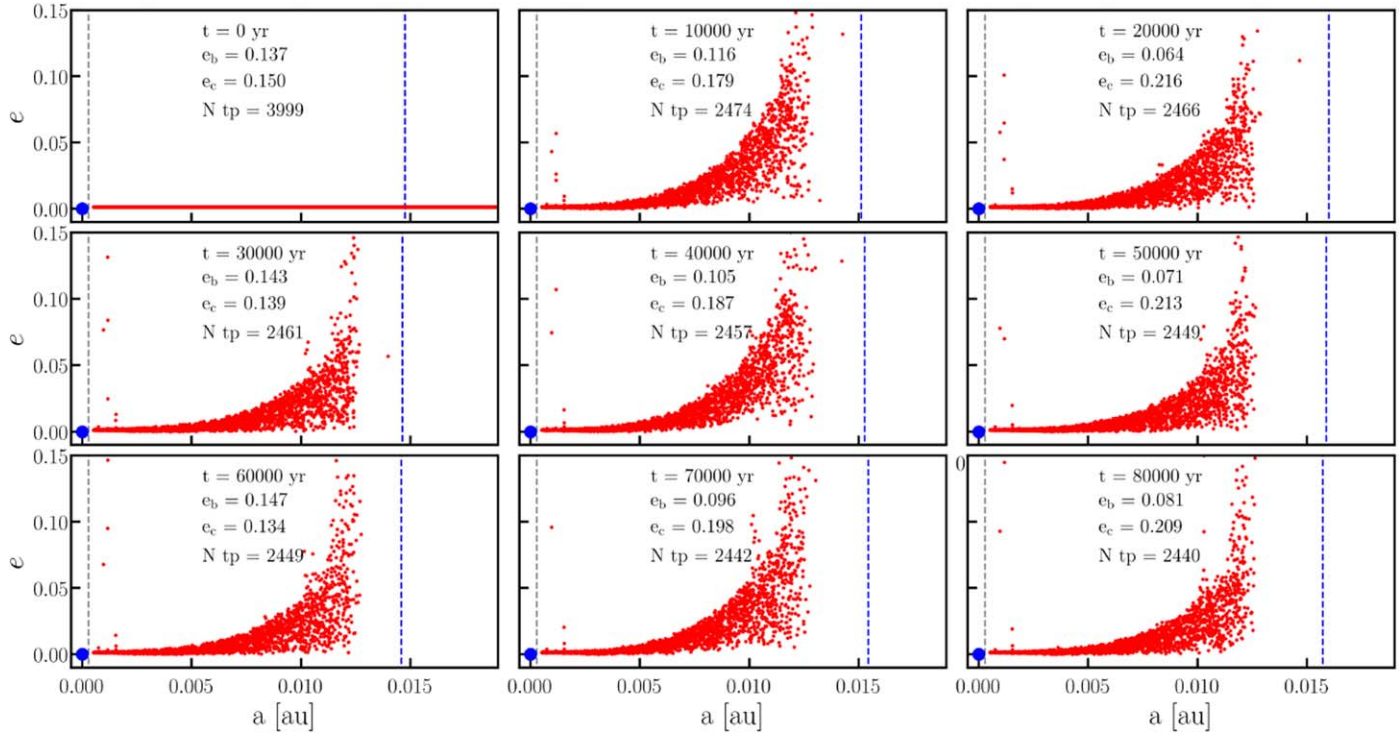

Figure D2. Same as in Figure D1, but for TOI-199 c.

ORCID iDs

Melissa J. Hobson https://orcid.org/0000-0002-5945-7975
Trifon Trifonov https://orcid.org/0000-0002-0236-775X
Thomas Henning https://orcid.org/0000-0002-1493-300X
Andrés Jordán https://orcid.org/0000-0002-5389-3944
Nestor Espinoza https://orcid.org/0000-0001-9513-1449
Rafael Brahm https://orcid.org/0000-0002-9158-7315
Jan Eberhardt https://orcid.org/0000-0003-3130-2768
Martin Schlecker https://orcid.org/0000-0001-8355-2107
Pascal José Torres Miranda https://orcid.org/0000-0003-0974-210X
Khalid Barkaoui https://orcid.org/0000-0003-1464-9276
Ilaria Carleo https://orcid.org/0000-0002-0810-3747
Karen A. Collins https://orcid.org/0000-0001-6588-9574
Knicole D. Colón https://orcid.org/0000-0001-8020-7121
Nicolas Crouzet https://orcid.org/0000-0001-7866-8738
Diana Dragomir https://orcid.org/0000-0003-2313-467X
Georgina Dransfield https://orcid.org/0000-0002-3937-630X
Tristan Guillot https://orcid.org/0000-0002-7188-8428
Maximilian N. Günther https://orcid.org/0000-0002-3164-9086
Saburo Howard https://orcid.org/0000-0003-4894-7271
Jon M. Jenkins https://orcid.org/0000-0002-4715-9460
Judith Korth https://orcid.org/0000-0002-0076-6239
David W. Latham https://orcid.org/0000-0001-9911-7388
Monika Lendl https://orcid.org/0000-0001-9699-1459
Jack J. Lissauer https://orcid.org/0000-0001-6513-1659
Christopher R. Mann https://orcid.org/0000-0002-9312-0073
Ismael Mireles https://orcid.org/0000-0002-4510-2268
George R. Ricker https://orcid.org/0000-0003-2058-6662
Richard P. Schwarz https://orcid.org/0000-0001-8227-1020
S. Seager https://orcid.org/0000-0002-6892-6948
Ramotholo Sefako https://orcid.org/0000-0003-3904-6754
Avi Shporer https://orcid.org/0000-0002-1836-3120
Chris Stockdale https://orcid.org/0000-0003-2163-1437
Olga Suarez https://orcid.org/0000-0002-3503-3617
Thiam-Guan Tan https://orcid.org/0000-0001-5603-6895
Amaury H. M. J. Triaud https://orcid.org/0000-0002-5510-8751
Roland Vanderspek https://orcid.org/0000-0001-6763-6562
Joshua N. Winn https://orcid.org/0000-0002-4265-047X
Bill Wohler https://orcid.org/0000-0002-5402-9613
George Zhou https://orcid.org/0000-0002-4891-3517

References

Abe, L., Gonçalves, I., Agabi, A., et al. 2013, A&A, 553, A49
Agol, E., Steffen, J., Sari, R., & Clarkson, W. 2005, MNRAS, 359, 567
Ballard, S., Fabrycky, D., Fressin, F., et al. 2011, ApJ, 743, 200
Baluev, R. V. 2009, MNRAS, 393, 969
Baranne, A., Queloz, D., Mayor, M., et al. 1996, A&AS, 119, 373
Barclay, T., Pepper, J., & Quintana, E. V. 2018, ApJS, 239, 2
Barnes, R. 2017, CeMDA, 129, 509
Boisse, I., Moutou, C., Vidal-Madjar, A., et al. 2009, A&A, 495, 959
Borucki, W. J., Koch, D., Basri, G., et al. 2010, Sci, 327, 977
Brahm, R., Espinoza, N., Jordán, A., et al. 2019, AJ, 158, 45
Brahm, R., Jordán, A., & Espinoza, N. 2017a, PASP, 129, 034002
Brahm, R., Jordán, A., Hartman, J., & Bakos, G. 2017b, MNRAS, 467, 971
Bressan, A., Marigo, P., Girardi, L., et al. 2012, MNRAS, 427, 127
Brown, T. M., Baliber, N., Bianco, F. B., et al. 2013, PASP, 125, 1031
Buchner, J., Georgakakis, A., Nandra, K., et al. 2014, A&A, 564, A125
Castelli, F., & Kurucz, R. L. 2003, in IAU Symp. 210, Modelling of Stellar Atmospheres, ed. N. Piskunov, W. W. Weiss, & D. F. Gray (San Francisco, CA: ASP), A20
Chabrier, G., Mazevet, S., & Soubiran, F. 2019, ApJ, 872, 51
Claret, A., & Bloemen, S. 2011, A&A, 529, A75
Collins, K. A., Kielkopf, J. F., Stassun, K. G., & Hessman, F. V. 2017, AJ, 153, 77
Dawson, R. I., & Johnson, J. A. 2018, ARA&A, 56, 175
Deck, K. M., Agol, E., Holman, M. J., & Nesvorný, D. 2014, ApJ, 787, 132
Dransfield, G., Mékarnia, D., Triaud, A. H. M. J., et al. 2022, Proc. SPIE, 12186, 121861F
Duncan, D. K., Vaughan, A. H., Wilson, O. C., et al. 1991, ApJS, 76, 383
Espinoza, N., & Jordán, A. 2015, MNRAS, 450, 1879
Espinoza, N., Kossakowski, D., & Brahm, R. 2019, MNRAS, 490, 2262
Feroz, F., Hobson, M. P., & Bridges, M. 2009, MNRAS, 398, 1601
Ferraz-Mello, S., Rodríguez, A., & Hussmann, H. 2008, CeMDA, 101, 171
Foreman-Mackey, D., Agol, E., Ambikasaran, S., & Angus, R. 2017, AJ, 154, 220
Foreman-Mackey, D., Hogg, D. W., Lang, D., & Goodman, J. 2013, PASP, 125, 306
Fox, C., & Wiegert, P. 2022, MNRAS, 516, 4684
Fulton, B. J., Petigura, E. A., Blunt, S., & Sinukoff, E. 2018, PASP, 130, 044504
Gaia Collaboration, Prusti, T., de Bruijne, J. H. J., et al. 2016, A&A, 595, A1
Gaia Collaboration, Vallenari, A., Brown, A. G. A., et al. 2023, A&A, 674, A1
Gladman, B. 1993, Icar, 106, 247
Gomes da Silva, J., Santos, N. C., Bonfils, X., et al. 2011, A&A, 534, A30
Grishin, E., Perets, H. B., Zenati, Y., & Michaely, E. 2017, MNRAS, 466, 276
Guillot, T., Abe, L., Agabi, A., et al. 2015, AN, 336, 638
Guillot, T., Fletcher, L. N., Helled, R., et al. 2022, arXiv:2205.04100
Guillot, T., & Morel, P. 1995, A&AS, 109, 109
Hobson, M. J., Brahm, R., Jordán, A., et al. 2021, AJ, 161, 235
Høg, E., Fabricius, C., Makarov, V. V., et al. 2000, A&A, 355, L27
Holman, M. J., & Murray, N. W. 2005, Sci, 307, 1288
Howard, S., & Guillot, T. 2023, A&A, 672, L1
Hubbard, W. B., & Marley, M. S. 1989, Icar, 78, 102
Jenkins, J. M. 2002, ApJ, 575, 493
Jenkins, J. M., Chandrasekaran, H., McCauliff, S. D., et al. 2010, Proc. SPIE, 7740, 77400D
Jenkins, J. M., Tenenbaum, P., Seader, S., et al. 2020, Kepler Data Processing Handbook: Transiting Planet Search KSCI-19081-003, Kepler Science Document
Jenkins, J. M., Twicken, J. D., McCauliff, S., et al. 2016, Proc. SPIE, 9913, 99133E
Jensen, E., 2013 Tapir: A Web Interface for Transit/Eclipse Observability, Astrophysics Source Code Library, ascl:1306.007
Jones, M. I., Brahm, R., Espinoza, N., et al. 2019, A&A, 625, A16
Jordán, A., Brahm, R., Espinoza, N., et al. 2020, AJ, 159, 145
Kaufer, A., Stahl, O., Tubbesing, S., et al. 1999, Msngr, 95, 8
Kempton, E. M. R., Bean, J. L., Louie, D. R., et al. 2018, PASP, 130, 114401
Kipping, D., & Yahalomi, D. A. 2023, MNRAS, 518, 3482
Kopparapu, R. K., Ramirez, R. M., SchottelKotte, J., et al. 2014, ApJL, 787, L29
Kreidberg, L. 2015, PASP, 127, 1161
Kunimoto, M., Winn, J., Ricker, G. R., & Vanderspek, R. K. 2022, AJ, 163, 290
Laskar, J., & Petit, A. C. 2017, A&A, 605, A72
Laurin, D., Hildebrand, A., Cardinal, R., Harvey, W., & Tafazoli, S. 2008, Proc. SPIE, 7010, 701013
Lee, M. H., & Peale, S. J. 2003, ApJ, 592, 1201
Li, J., Tenenbaum, P., Twicken, J. D., et al. 2019, PASP, 131, 024506
Mankovich, C. R., & Fuller, J. 2021, NatAs, 5, 1103
Mayor, M., Pepe, F., Queloz, D., et al. 2003, Msngr, 114, 20
McCully, C., Volgenau, N. H., Harbeck, D.-R., et al. 2018, Proc. SPIE, 10707, 107070K
Mékarnia, D., Guillot, T., Rivet, J. P., et al. 2016, MNRAS, 463, 45
Müller, S., & Helled, R. 2023, A&A, 669, A24
Nesvorný, D., Kipping, D. M., Buchhave, L. A., et al. 2012, Sci, 336, 1133
Noyes, R. W., Hartmann, L. W., Baliunas, S. L., Duncan, D. K., & Vaughan, A. H. 1984, ApJ, 279, 763
Parmentier, V., Guillot, T., Fortney, J. J., & Marley, M. S. 2015, A&A, 574, A35
Pecaut, M. J., & Mamajek, E. E. 2013, ApJS, 208, 9
Pepe, F., Mayor, M., Rupprecht, G., et al. 2002, Msngr, 110, 9
Queloz, D., Henry, G. W., Sivan, J. P., et al. 2001a, A&A, 379, 279
Queloz, D., Mayor, M., Udry, S., et al. 2001b, Msngr, 105, 1

Ricker, G. R., Winn, J. N., Vanderspek, R., et al. 2015, JATIS, 1, 014003
Rodrigo, C., & Solano, E. 2020, in XIV.0 Scientific Meeting (Virtual) of the Spanish Astronomical Society (Bilbao: SEA), 182
Rodrigo, C., Solano, E., & Bayo, A. 2012, SVO Filter Profile Service Version 1.0, IVOA
Sarkis, P., Mordasini, C., Henning, T., Marleau, G. D., & Mollière, P. 2021, A&A, 645, 79
Schlecker, M., Kossakowski, D., Brahm, R., et al. 2020, AJ, 160, 275
Schmider, F.-X., Abe, L., Agabi, A., et al. 2022, Proc. SPIE, 12182, 121822O
Skilling, J. 2004, in AIP Conf. Ser. 735, Bayesian Inference and Maximum Entropy Methods in Science and Engineering, ed. R. Fischer, R. Preuss, & U. V. Toussaint (Melville, NY: AIP), 395
Skrutskie, M. F., Cutri, R. M., Stiening, R., et al. 2006, AJ, 131, 1163
Smith, J. C., Stumpe, M. C., Van Cleve, J. E., et al. 2012, PASP, 124, 1000
Southworth, J. 2011, MNRAS, 417, 2166
Speagle, J. S. 2020, MNRAS, 493, 3132
Stassun, K. G., Oelkers, R. J., Paegert, M., et al. 2019, AJ, 158, 138
Stumpe, M. C., Smith, J. C., Catanzarite, J. H., et al. 2014, PASP, 126, 100
Stumpe, M. C., Smith, J. C., Van Cleve, J. E., et al. 2012, PASP, 124, 985
Sullivan, P. W., Winn, J. N., Berta-Thompson, Z. K., et al. 2015, ApJ, 809, 77
Tayar, J., Claytor, Z. R., Huber, D., & van Saders, J. 2022, ApJ, 927, 31
Tokovinin, A. 2018, PASP, 130, 035002
Tokovinin, A., Fischer, D. A., Bonati, M., et al. 2013, PASP, 125, 1336
Trifonov, T., 2019 The Exo-Striker: Transit and Radial Velocity Interactive Fitting Tool for Orbital Analysis and N-body Simulations, Astrophysics Source Code Library, ascl:1906.004
Trifonov, T., Brahm, R., Espinoza, N., et al. 2021, AJ, 162, 283
Trifonov, T., Lee, M. H., Kürster, M., et al. 2020, A&A, 638, A16
Twicken, J. D., Catanzarite, J. H., Clarke, B. D., et al. 2018, PASP, 130, 064502
Wisdom, J., & Holman, M. 1991, AJ, 102, 1528
Ziegler, C., Tokovinin, A., Briceño, C., et al. 2020, AJ, 159, 19